

# Solar and thermal radiation pressure modelling for improving the GOCE horizontal wind dataset

Hładczuk, N. A.; van den IJssel, J.; Jacobs, F.; Siemes, C.; Visser, P.

DOI

10.1016/j.asr.2025.09.043

**Publication date** 

**Document Version** Final published version

Published in

Advances in Space Research

Citation (APA)

Hładczuk, N. A., van den IJssel, J., Jacobs, F., Siemes, C., & Visser, P. (2025). Solar and thermal radiation pressure modelling for improving the GOCE horizontal wind dataset. *Advances in Space Research*, *76*(11), 6899-6917. https://doi.org/10.1016/j.asr.2025.09.043

Important note

To cite this publication, please use the final published version (if applicable). Please check the document version above.

Copyright

Other than for strictly personal use, it is not permitted to download, forward or distribute the text or part of it, without the consent of the author(s) and/or copyright holder(s), unless the work is under an open content license such as Creative Commons.

Please contact us and provide details if you believe this document breaches copyrights. We will remove access to the work immediately and investigate your claim.





#### Available online at www.sciencedirect.com

# **ScienceDirect**

Advances in Space Research 76 (2025) 6899-6917

ADVANCES IN SPACE RESEARCH (a COSPAR publication)

www.elsevier.com/locate/asr

# Solar and thermal radiation pressure modelling for improving the GOCE horizontal wind dataset

N.A. Hładczuk\*, J. van den IJssel, F. Jacobs, C. Siemes, P. Visser

Department of Astrodynamics and Space Missions, Faculty of Aerospace Engineering, Delft University of Technology, Kluyverweg 1, Delft 2629 HS, the Netherlands

Received 20 May 2025; received in revised form 12 September 2025; accepted 15 September 2025 Available online 19 September 2025

#### Abstract

The Gravity Field and Steady-State Ocean Circulation Explorer (GOCE) satellite, which operated at an altitude of ~250km, provided neutral thermosphere mass density and crosswind observations in the dawn-dusk sectors throughout most of its operational lifetime (2009–2013). As a result of its Sun-synchronous orbit, GOCE's large solar panels remained at a near-perpendicular angle to the incoming solar radiation, leading to a significant radiation pressure acceleration. In this research, we focused on revisiting and reprocessing GOCE thermosphere mass density and crosswind data. We selected the coefficients describing the thermo-optical surface properties and employed a high-fidelity satellite geometry in a ray-racing simulation. Additionally, we distinguished between the solar flux in the visible and infrared bands and introduced a model for the satellite's thermal emission. The availability of the in situ thermistor measurements allowed for the validation of the thermal model. Moreover, we replaced the Level-1b ion thruster data with raw telemetry, filling multiple data gaps. We analysed how incremental improvements in the radiation pressure modelling affected the observed crosswind speed. By replacing the panel model with the high-fidelity satellite geometry, the crosswind speed decreased up to 5 ms<sup>-1</sup>. The biggest difference reduction of  $40 \text{ms}^{-1}$  resulted from introducing the thermal model. Splitting the solar flux further decreases the observed crosswind speed by up to 8ms<sup>-1</sup>. The reduction in crosswind speed was most prominent during the first years of the mission when the solar activity was low. We compared the newly processed GOCE zonal wind data with respect to the most recent previous release. We observed a median absolute deviation decrease of 10 ms<sup>-1</sup> around the south magnetic pole in the dawn sector. The yearly consistency of low-latitude zonal winds did not change significantly. The main obstacle in quantifying the improvement compared to the previous crosswind dataset stemmed from the fact that the previous and new datasets were generated with different crosswind estimation algorithms. The difference in thermosphere density compared to previously published datasets is minor since the effect of radiation pressure is most prominent in the cross-track direction. Finally, we verified the assumption about the energy accommodation coefficient of 0.82 and concluded that it remains valid after implementing the radiation pressure modelling improvements.

© 2025 The Author(s). Published by Elsevier B.V. on behalf of COSPAR. This is an open access article under the CC BY license (http://creativecommons.org/licenses/by/4.0/).

Keywords: Thermosphere; Horizontal winds; Satellite thermal emission; Radiation pressure; GOCE

*E-mail addresses*: N.A.Hladczuk@tudelft.nl (N.A. Hładczuk), J.A.A. vandenIJssel@tudelft.nl (J. van den IJssel), F.Jacobs@tudelft.nl (F. Jacobs), C.Siemes@tudelft.nl (C. Siemes), P.N.A.M.Visser@tudelft.nl (P. Visser).

#### 1. Introduction

The Gravity Field and Steady-State Ocean Circulation Explorer (GOCE) was the first European Space Agency (ESA) Core Earth Explorer Mission, launched in March 2009 and operated until November 2013 (Floberghagen et al., 2011). Its primary objective was to map Earth's gravity field and model the geoid height with unprecedented

<sup>\*</sup> Corresponding author.

accuracy. The mission successfully achieved a range of multidisciplinary scientific goals, including applications in geodesy, geophysics, oceanography, glaciology, and climate research.

GOCE flew in a near-circular, Sun-synchronous dusk-dawn orbit with an inclination of 96.5°. The satellite altitude was 270 km at the beginning of the mission and was lowered to 240 km by the end of operations. This orbit was selected to provide optimal Earth coverage while minimizing the time spent in eclipses. As a result, one side of the satellite was always directed toward the Sun while the other was never directly illuminated by sunlight. The satellite's subsystems were powered by four body-mounted and two wing-mounted solar panels equipped with triplejunction gallium arsenide (GaAs) solar cells, which made GOCE the first gravimetry mission to use this technology.

GOCE was equipped with a Satellite-to-Satellite Tracking Instrument, which was used to determine the position and velocity, and star trackers that provided information on attitude (Drinkwater et al., 2007). Maintaining the satellite's low operational altitude was made possible by a dragfree control system enabled by ion propulsion (Andreis and Canuto, 2005). The core instrument onboard the spacecraft was the Electrostatic Gravity Gradiometer (EGG), measuring the gravity gradients along GOCE's orbit. The EGG consisted of three pairs of three-axis, servo-controlled accelerometers, providing independent measurements of the gravity gradient components (Drinkwater et al., 2007).

GOCE's low altitude, where aerodynamic accelerations are significant, provided unique conditions for obtaining highly accurate crosswind estimates. The availability of four years of GOCE wind data facilitated a number of studies. Because of its near-polar orbit and mostly fixed local time, GOCE winds remain uncontaminated by local solar time variations, providing an opportunity to study seasonal dependencies. GOCE data allowed the analysis of the spatial and temporal variability of thermospheric zonal winds (Molina and Scherliess, 2023)), helped to identify wind jets (Liu et al., 2016), and gave insights into intraannual oscillations in upper thermospheric winds (Dhadly et al., 2020). Furthermore, GOCE cross-track wind data has been assimilated into wind models, effectively filling gaps in the twilight regions that are typically inaccessible through ground-based measurements such as Fabry-Perot Interferometers (Drob et al., 2015). However, studies also revealed that GOCE winds obtained from gravitational accelerations show substantial offsets compared to other space-based and ground-based observations (Dhadly et al. (2017, 2018)). Moreover, characteristic jumps in GOCE winds have been identified at the locations where the satellite entered and exited eclipses (Doornbos et al., 2014).

The most recent version of GOCE data, prior to the one presented here, was version 2.0 in the ESA GOCE Data Collections Website, which is the exact same dataset as version V01, found in http://thermosphere.tudelft.nl. This dataset, consisting of both vertical and horizontal winds,

was produced using an algorithm based on linear and angular accelerations as described in Visser et al. (2019). The algorithm relies on the measured accelerations to calculate a net force and torque acting on the satellite. Therefore, the algorithm output is a pair of wind datasets, one force-derived and one torque-derived, which, after applying an offset correction, results in a final wind estimate.

The derivation of density and winds from the satellite's accelerometer data relies on the precise modelling of non-gravitational forces. For GOCE, the thrust exerted by the drag-free control system acts as an additional acceleration, which must first be added to the calibrated acceleration. Afterwards, the aerodynamic acceleration is obtained by subtracting the radiation pressure from the remaining signal. Likewise version V01, this study uses a high-fidelity GOCE geometry (March et al., 2019a) to model the aerodynamic drag.

This study aims to provide new insights into GOCE horizontal winds by reprocessing all data using enhanced processing standards and models. Crosswind data are particularly sensitive to acceleration modelling errors in the cross-track direction, where the main contributors are solar radiation pressure and the satellite's thermal emission. To take advantage of the high-fidelity geometry for radiation pressure modelling, we assigned appropriate thermo-optical surface properties to each geometry element. Such a model is then used in ray-tracing simulations to determine radiation pressure force coefficients. Ravtracing is an efficient method for modelling the momentum exchange between incident radiation and the satellite surface while accounting for self-shadowing and multiple reflections. To optimize computational efficiency, the raytracing simulation is performed once for all directions of incidence, and the resulting coefficients are stored in a lookup table (Siemes et al., 2023; Hładczuk et al., 2024). This approach has been already adopted by various research groups (Bhattarai et al., 2022; Ziebart, 2004; Li et al., 2018).

In the standard approach to Solar Radiation Pressure (SRP) modelling, the solar spectrum is assumed to be fully in the visible wavelength range. However, in reality, the interaction between the solar flux and the satellite surface is frequency-dependent. This aspect is often neglected or simplified due to uncertainties in the satellite surface properties. In this study, we divided the solar flux between the two main contributing wavelengths, infrared and visible, following a similar approach as Vielberg and Kusche (2020).

In addition to the SRP, the acceleration due to the satellite's thermal emission is the second largest contributor to the cross-track radiation pressure acceleration, accounting for one-fourth of the signal. Typically, the thermal effect is either neglected or modelled as simple instantaneous heat re-emission (Montenbruck et al., 2015; Vielberg and Kusche, 2020). State-of-the-art models account for transient heat conduction and characterize the heat exchange using thermal control parameters such as heat capacity, conductivity, and heat generation by the inner parts (Wöske et al., 2019; Siemes et al., 2023). Some studies additionally account for the efficiency of the solar arrays, defined as the amount of absorbed radiation converted into electricity instead of heat (Wang et al., 2023; Adhya, 2005; Hładczuk et al., 2024).

In this study, we provide new insights into radiation pressure modelling by applying a ray-tracing technique and revisiting the selection of the thermo-optical properties of satellite materials. For a more realistic SRP model, we accounted for the visible and infrared contributions of the solar spectrum. We proposed a thermal model based on the transient heat conduction and accounted for the heat transfer through the satellite wing - a distinctive feature of the GOCE design. Finally, we validated the choice of model control parameters by comparing the modelled temperatures to the readings from the GOCE thermistors.

The paper is structured as follows. First, in Section 2, we discuss the input data. Then, in Section 3, we explain the methodology of the radiation pressure modelling, including thermal emission and heat transfer through the satellite wing. Section 4 presents the results, including new crosswind estimates. Finally, Section 5 discusses the conclusions and opportunities for future work.

#### 2. Data

#### 2.1. GOCE data

All GOCE Level-1b and Level-2 data collections, including the temperature readings, are freely available on ESA GOCE Data Collections Website. The GOCE satellite operated under drag-free control, using an ion thruster to continuously compensate for atmospheric drag in the in-flight direction. Previously published GOCE datasets were based on Level-1b ion thruster data. In this work, we used raw telemetry thruster data instead. This allowed us to fill numerous data gaps (280 gaps longer than 5 min). For the remaining data products, we used the most recent version of the Level-1b data. Additionally, we updated the accelerometer bias estimation (Visser and van den IJssel, 2016) to be consistent with that version of the accelerometer data.

To process GOCE density and crosswind data, we utilize the following models: NRLMSISE-00 model (Picone et al., 2002) to obtain the atmospheric composition and temperature and HWM07 (Drob et al., 2008) to account for in-track wind.

# 2.2. Thermistors data

Each panel of GOCE was equipped with a pair of Rosemount 0118MF temperature sensors, as shown on Fig. 1. Unlike GRACE-FO (Hładczuk et al., 2024) and Swarm, GOCE's thermal sensors were installed on the rear side of each panel, making them unsuitable for direct use in thermal modelling. However, these thermistors can still

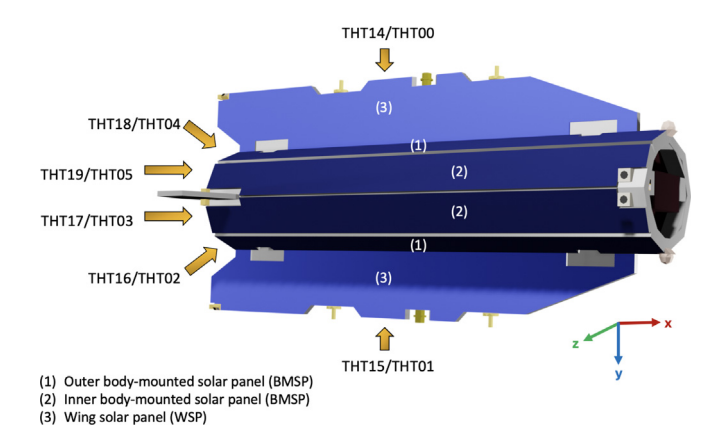


Fig. 1. Approximate locations of the GOCE thermistor pairs on each panel. The pairs named THT17/THT03 and THT19/THT05 were mounted on the inner body-mounted solar panels (BMSP), whereas THT16/THT02 and THT18/THT04 were mounted on the outer BMSP. The sensors THT14/THT00 and THT15/THT01 were placed on the wing solar panels (WSP). Note that the thermistors are located on the rear side of the panels.

serve as reference temperature. Being located beneath the panels and thus better insulated, their temperature readings record less extreme values than the outer temperatures we aim to model. An exception is a thermistor located on the rear side of the wing, which can be directly used to compare modelled and measured temperatures.

Fig. 2 shows the temperature variation during a few orbits as well as the orbit mean temperature. We compared the temperature readings from thermistors on the same panel throughout the mission lifespan to examine thermal gradients across the surface. The difference within the thermistor measurements was at most  $10~^{\circ}\text{C}$  in the sunlight and  $20~^{\circ}\text{C}$  in the eclipse.

# 2.3. High-fidelity geometry model

For GOCE aerodynamic and radiation pressure modelling, we utilised the detailed geometry model illustrated in Fig. 1, similar to the ones developed for CHAMP, Swarm, and GRACE. The model, which consists of 2474 mesh triangles, was created using CAD software and constructed from technical drawings and pre-launch images (March et al., 2019a). The GOCE high-fidelity geometry model was used as input for a ray-tracing simulation to calculate radiation pressure force coefficients. To achieve this, we enhanced the model by assigning surface material properties to each mesh element. These properties were defined for both visible and infrared wavelengths. Details on the selection of surface coefficients are provided in Section 4.2.

#### 3. Methodology

GOCE was equipped with the Electrostatic Gravity Gradiometer consisting of three orthogonal pairs of accelerometers, providing independent measurements of the gravity gradient components in the along-track,

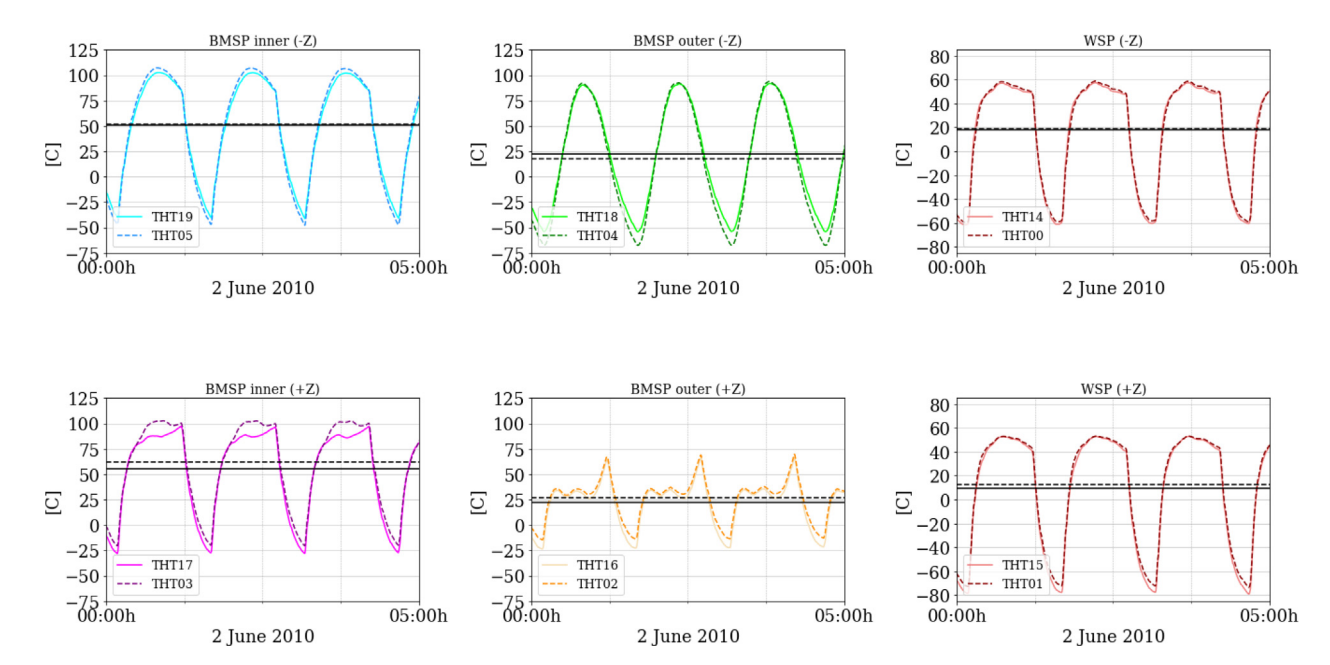


Fig. 2. Temperature measurements of the thermistors placed on the same panel. The horizontal black lines show the orbit mean temperature of the corresponding thermistors. Acronym BMSP refers to the body-mounted solar panels, whereas WSP refers to the wing solar panels.

cross-track and vertical directions. Since GOCE accelerometers do not coincide with the satellite centre of mass, we are using the so-called common mode acceleration, which is obtained by averaging the accelerations measured along the corresponding axis of the gradiometer (Visser and van den IJssel, 2016).

To retrieve the aerodynamic signal,  $a_{\rm aero}$ , we subtract the other nongravitational accelerations from the calibrated common-mode accelerations  $a_{\rm cal}$ . These other nongravitational accelerations consist of solar radiation pressure (SRP),  $a_{\rm srp}$ , Earth albedo,  $a_{\rm alb}$ , Earth infrared radiation,  $a_{\rm ir}$ , and thermal acceleration,  $a_{\rm te}$ . The continuous thrust applied by the ion thruster as part of the drag-free control system acted as an additional acceleration,  $a_{\rm thr}$ , which cancelled the aerodynamic acceleration in the thrust direction. Therefore, we must add  $a_{\rm thr}$  to  $a_{\rm cal}$  to obtain the aerodynamic acceleration  $a_{\rm aero}$ .

This amounts to

$$\boldsymbol{a}_{\text{aero}} = \boldsymbol{a}_{\text{cal}} - \boldsymbol{a}_{\text{srp}} - \boldsymbol{a}_{\text{ir}} - \boldsymbol{a}_{\text{alb}} - \boldsymbol{a}_{\text{te}} - \boldsymbol{a}_{\text{thr}}. \tag{1}$$

The neutral mass density  $\rho$  can be calculated from the acceleration along the satellite's x-axis  $a_{aero,x}$  by

$$\rho = \frac{2 m a_{\text{aero},x}}{C_{\text{aero},x} V_{rel}^2},\tag{2}$$

where m denotes the satellite mass, and  $V_{rel}$  is the satellite's velocity relative to the atmosphere. Since the satellite's x and y-axes are approximately aligned with the along-track and cross-track directions, respectively, we refer to the accelerations in these directions as the along-track and cross-track accelerations. The term  $C_{aero,x}$  is the x-component of the aerodynamic coefficient vector (approximately aligned with the flight direction) intrinsically multi-

plied by the reference area. Due to the drag-free flight, information about GOCE's density primarily comes from thruster activation data.

Both neutral mass density and crosswind estimations rely on the accurate modelling of aerodynamic acceleration. Consequently, the errors in crosswind data arise from inaccuracies in the cross-track acceleration, with radiation pressure being a significant contributor. The effect of the radiation pressure mismodelling has been already studied for higher-altitude satellites such as Swarm (van den IJssel et al., 2020), GRACE (Wöske et al., 2019), and GRACE-FO (Siemes et al., 2023; Hładczuk et al., 2024).

Fig. 3 shows the ratio between the size of radiation pressure acceleration components with respect to the size of the aerodynamic acceleration. The magnitude of accelerations was calculated using a sliding one-month window root mean square (RMS). At GOCE altitude, during the early phase of the mission when the solar activity was low, the solar radiation pressure acceleration had magnitude up to 1% of the aerodynamic acceleration in the along-track direction (Fig. 3.a) and 50% in cross-track direction (Fig. 3.b). The reason for the small ratio of radiation pressure to aerodynamic acceleration in the along-track direction compared to the cross-track direction is twofold: drag, which acts approximately in the along-track direction, is much larger than the side forces acting in the cross-track direction. Second, the radiation pressure acceleration in the along-track direction is much smaller than that in the cross-track direction because of the dawndusk orbit.

The next largest contribution stems from thermal emission, with a magnitude of approximately one-fifth of the aerodynamic acceleration in the cross-track direction.

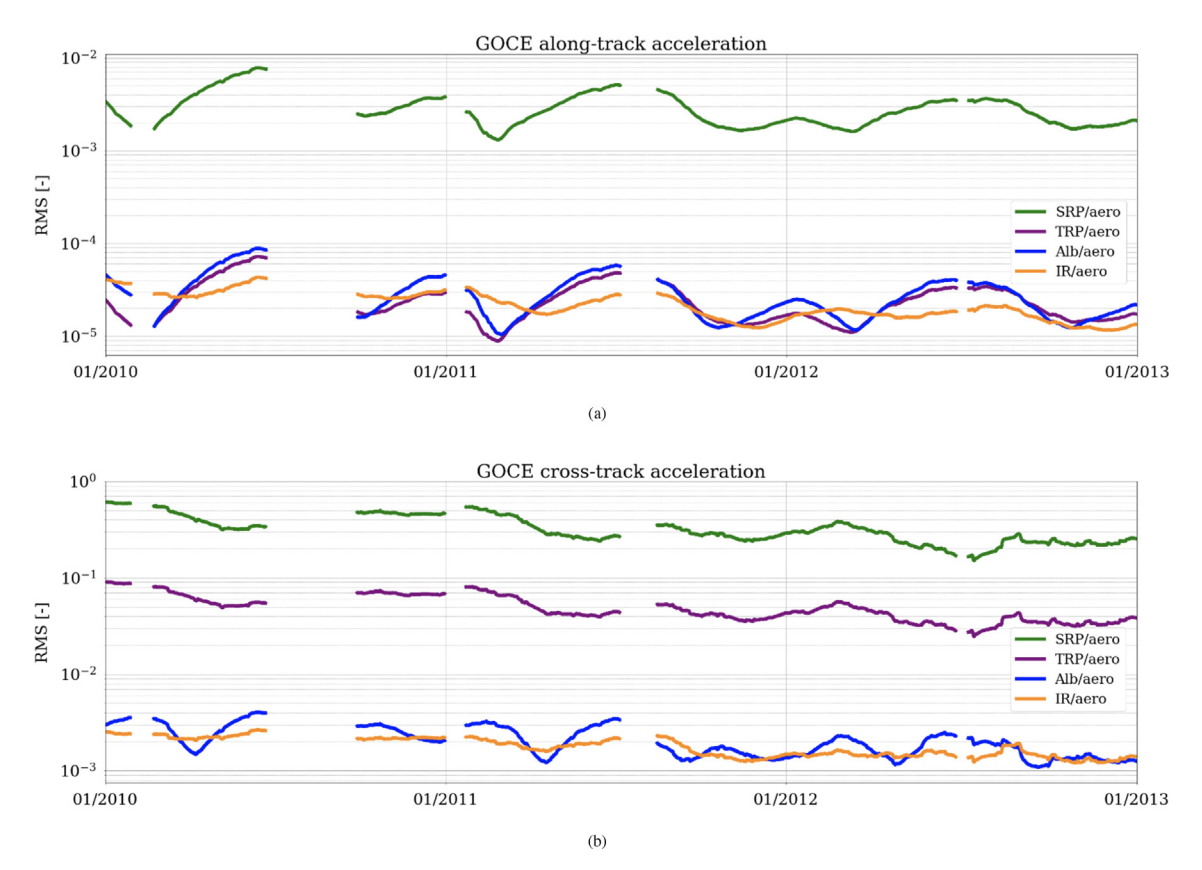


Fig. 3. Ratio between the radiation pressure components and the aerodynamic coefficient (aero). The radiation pressure components are: solar radiation pressure (SRP), thermal radiation pressure (TRP), Earth albedo (Alb), and Earth infra-red radiation (IR). The magnitude of accelerations was calculated using a sliding one-month window root mean square (RMS).

The accelerations due to albedo and Earth's infrared emission have a negligible impact on the cross-track acceleration. As solar activity increases towards the end of the mission, the ratio between the radiation pressure acceleration component and the aerodynamic acceleration decreases.

Apart from the radiation pressure, additional error sources are accelerometer cross-track bias and accelerometer scale factor errors, as well as the misalignment of the thrust vector.

# 3.1. Radiation pressure modelling

The radiation pressure acceleration is defined as

$$\boldsymbol{a}_{\text{ext}}(\alpha,\beta) = \frac{1}{m} \int_{\lambda} P_{\text{ext}}(\alpha,\beta,\lambda) \boldsymbol{C}(\alpha,\beta,\lambda) d\lambda$$
 (3)

where m is the satellite mass and  $P_{\rm ext}$  is an external radiation pressure source such as the Sun (solar radiation pressure) or the Earth (infrared radiation and albedo). The coefficient C depends on the radiations's wavelength  $\lambda$ , and the angles  $\alpha$  and  $\beta$ , which describe the orientation of the satellite to incident radiation. The angles can be derived using a unit vector fixed to the satellite reference frame,  $\mathbf{u}_{\rm sat}$ , pointing from the radiation source towards the satellite:

$$\mathbf{u}_{\text{sat}} = \begin{bmatrix} u_x \\ u_y \\ u_z \end{bmatrix}, \quad \alpha = \arcsin(u_z), \quad \beta = \arctan_2(u_y, -u_x).$$
 (4)

The solar radiation pressure  $P_{\rm srp}(\lambda)$  at the position of the satellite is calculated using the solar radiation pressure at one astronomical unit,  $P_{\rm IAU}$ , and the distance from the Sun to the satellite  $\|\mathbf{r}_{\rm sat} - \mathbf{r}_{\rm Sun}\|$ :

$$P_{\rm srp}(\lambda) = \left(\frac{1 \text{AU}}{\|\mathbf{r}_{\rm sat} - \mathbf{r}_{\rm Sun}\|}\right)^2 P_{1 \text{AU}}(\lambda). \tag{5}$$

The solar radiation pressure at 1AU is commonly approximated by the ratio of the mean solar constant  $\Phi = 1361 \, \mathrm{W \, m^{-2}}$  to the speed of light c, (i.e.  $P_{1\mathrm{AU}} = \Phi/c = 4.53 \, \mu \, \mathrm{N \, m^{-2}}$ ). The mean solar constant was estimated using CERES data from 2000 to 2024. We found the temporal variation in the solar flux to have a negligible effect on the acceleration and, therefore, did not account for it in this work.

The solar constant is an average of the Sun's energy flux integrated over all wavelengths. We accounted for dependency on both visible and infrared frequency bands of the solar spectrum, departing from the standard approach that considers only the visible range. Since the satellite material properties are typically available only for the visible and infrared wavelengths, we approximate the total

flux by evenly distributing it between these bands (50% visible and 50% infrared). This method is similar to the extended SRP model proposed by Vielberg and Kusche (2020). Subsequently, we introduced the solar constant values for the visible and the infrared parts of the spectrum  $\Phi_{vis} = 680.5 \, \mathrm{W \, m^{-2}}$  and  $\Phi_{ir} = 680.5 \, \mathrm{W \, m^{-2}}$ , respectively.

To model the visible and infrared radiation pressure coefficient  $C_{vis}$  and  $C_{ir}$ , we augmented the GOCE aerodynamic model with thermo-optical surface properties and employed a ray-tracing technique. The advantage of this method is that it accounts for both self-shadowing and multiple reflections. The details on the ray-tracing algorithm can be found in Siemes et al. (2023) and Hładczuk et al. (2024). The method was used to calculate the acceleration due to solar radiation pressure, Earth's infrared radiation, and albedo. For albedo and Earth's thermal emission, we use monthly averaged maps based on Earth Radiation Budget Experiment (ERBE) satellite data (Doornbos et al., 2014). We evaluated the impact of replacing the ERBE data with more precise Clouds and Earth's Radiant Energy System (CERES). However, the differences at the acceleration level were negligible given the size of the radiation pressure acceleration contributions, as shown in Fig. 3.

#### 3.2. Thermal emission modelling

The implemented thermal model is based on independent panels outlining the GOCE satellite's geometry. The net heat exchange of an individual panel *j* is

$$\dot{Q}_i = (1 - e_i) \dot{Q}_{\text{abs},i} - \dot{Q}_{\text{emit},i} - \dot{Q}_{\text{cond},i}, \tag{6}$$

where  $\dot{Q}_{{\rm abs},j}$  denotes absorbed radiation,  $\dot{Q}_{{\rm emit},j}$  emitted radiation, and  $\dot{Q}_{{\rm cond},j}$  conductive heat exchange either with the satellite body or through the satellite wing depending on the panel. The efficiency  $e_j$  represents the fraction of absorbed energy converted into electricity (Hładczuk et al., 2024; Wang et al., 2023).

Since the panel model does not account for self-shadowing, using such a model to account for the satellite's thermal emission may introduce errors. Therefore, we implemented a modified version of the panel model of Dumontel (2010), estimating the illuminated area of the Sun-opposing horizontal stabiliser instead of using the total area. This was possible due to GOCE's distinctive orbit, where the orientation of the Sun-facing and Sun-opposing panels remains roughly fixed.

In the first step of numerical implementation, panels absorb the incoming radiation originating from the Sun and Earth, including albedo. Our calculations account for the dependency on both visible and infrared parts of the solar spectrum. The change in heat due to absorbed radiation is

$$\dot{Q}_{\text{abs},j} = (\Phi_{vis} c_{\text{vis},a,j} + \Phi_{ir} c_{\text{ir},a,j}) A_j \cos \theta_j, \tag{7}$$

where  $c_{\text{vis},a,j}$  is the absorption coefficient for visible light,  $c_{\text{ir},a,j}$  is the absorption coefficient for infrared radiation,  $A_j$  is the area of the panel, and  $\theta_j$  is the angle between the panel's outward normal and the vector from the satellite to the radiation source. The heat absorption is followed by heat loss toward space following the Stefan–Boltzmann law.

$$\dot{Q}_{\text{emit},j} = A_j c_{\text{ir},a,j} \sigma T_j^4, \tag{8}$$

where  $T_j$  is the absolute temperature of the satellite panels and  $\sigma$  is the Stefan–Boltzmann constant.

In the case of the GOCE satellite, two scenarios can be distinguished. For the panels attached directly to the satellite body, thermal conduction  $k_j$  between the satellite walls and the inner body  $T_{\text{body}}$  occurs

$$\dot{Q}_{\text{cond},j} = k_j (T_j - T_{\text{body}}). \tag{9}$$

The heat change of the satellite body  $\dot{Q}_{\rm body}$  is then defined as

$$\dot{Q}_{\text{body}} = \dot{Q}_{\text{gen}} + \sum_{j} \dot{Q}_{\text{cond},j},\tag{10}$$

where  $\dot{Q}_{\rm gen}$  stands for the internal heat generated by the payload and satellite systems.

The second scenario concerns elements where the surface area connected to the satellite body is significantly smaller than the panel area, such as the satellite wings or the stabilizers. In these cases, instead of the thermal conduction towards the satellite body we consider the heat transfer through the panel

$$\dot{Q}_{\text{cond},j} = \frac{(T_{j_1} - T_{j_2})}{R_i},\tag{11}$$

where  $T_{j_1}$  and  $T_{j_2}$  denote two sides of the panel, and  $R_j$  is the panel's thermal resistance, noting that  $R_j = k_j^{-1}$ .

The panels and body temperatures are updated by

$$T_j(t + \Delta t) = T_j(t) + \frac{\dot{Q}_j}{C_i} \Delta t, \tag{12}$$

and

$$T_{\text{body}}(t + \Delta t) = T_{\text{body}}(t) + \frac{\dot{Q}_{\text{body}}}{C_{\text{body}}} \Delta t, \tag{13}$$

where  $C_j$  and  $C_{\text{body}}$  are the thermal capacity of the panels and the satellite body, t is time, and  $\Delta t$  is the time difference to the next time step.

In the last step, the thermal radiation pressure acceleration

$$\boldsymbol{a}_{\text{te}} = -\frac{2}{3} \sum_{j} \frac{\dot{Q}_{\text{emit},j}}{m c} \boldsymbol{n}_{j} \tag{14}$$

is calculated, where  $n_j$  is the outer panel normal of the j-th surface element.

#### 3.2.1. Thermal model control parameters

The proposed thermal model includes the following control parameters: heat capacitance of the panels  $(C_j)$  and the body  $(C_{body})$ , thermal resistance of the panels  $(R_j)$ , efficiency of the solar cells  $(e_j)$ , and internally generated heat  $(\dot{Q}_{gen})$ . Due to the characteristics of the GOCE orbit, the geometry can be divided into Sun-facing elements (solar panels) and Sun-opposing elements (insulation foil). Since the main thermal impact originates from the illuminated parts of the satellite (Eq. 8), we focus in this section solely on describing the thermal properties of the Sun-facing panels.

The GOCE satellite was equipped with four body-mounted solar panels, consisting of two larger inner panels and two smaller outer panels, along with two wing solar panels, as shown in Fig. 1. GOCE solar panels contain triple-junction Gallium Arsenide (GaAs) solar cells, similar in design to those used on the Swarm and GRACE-FO missions (Kornfeld et al., 2019).

The efficiency of the solar cells decreases with the temperature, as shown in Fig. 4. Since the efficiency is only relevant when the solar panels are sunlit, we consider the following temperatures: For the satellite front wings, we assume a temperature of around 70 °C, for the outer body-mounted panels 100 °C, and for the inner body-mounted panels 140 °C, which translates to cell efficiencies of 23%, 21%, and 18%, respectively. These temperatures are consistent with those predicted by our thermal model. For reference efficiency, we used the values provided at the beginning-of-life. However, it should be noted that the difference in the beginning and end-of-life efficiency provided by the documentation is less than 1%.

The area of a single solar cell is 30.18 cm<sup>2</sup> (Dutch Space, 2005) and the number of cells per panel is 676 for each of the WSP, 338 for each of the outer BMSP and 390 for each of the inner BMSP (Dutch Space, 2005). The effective efficiency of the whole panel was estimated by calculating the packing factor, taking into account the area covered by the photovoltaic cells (Hładczuk et al., 2024). For the BMSP, this yields the effective efficiencies of 10% and 11% for the inner and outer panels, respectively (packing factors:

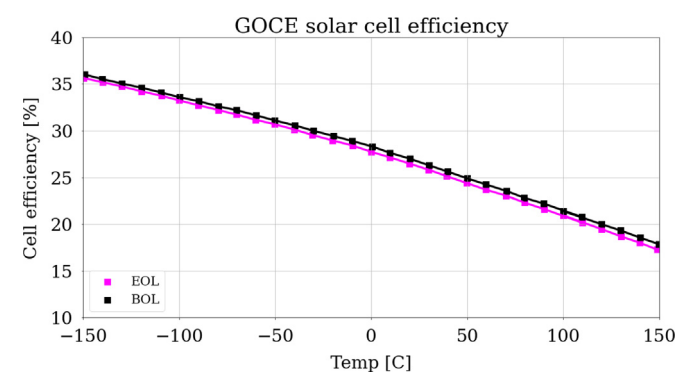


Fig. 4. Efficiency of GOCE solar cells in the beginning-of-life (BOL) and end-of-life (EOL) provided in the technical documentation (Dutch Space, 2006).

0.56 and 0.53), and 16% for the WSP (packing factor 0.72). It is worth pointing out that cell efficiency varies slightly throughout the mission lifespan, and manufacturers usually define them separately for the beginning and end of life (Fig. 4). However, in this work, we consider this change negligible.

The thermal capacitance determines the ability of the panel to store heat and depends on the panel temperature. The values for the BMSP and WSP were based on the information provided in the technical documentation (Dutch Space, 2006). Fig. 5 shows temperature-dependent thermal capacitance of the front and rear sides of the wing. The temperature of these panels remains fairly constant for GOCE, due to the Sun-synchronous orbit, with the exception of the eclipse passes. In this work, we use a fixed value selected in accordance with the temperature that the satellite reaches in sunlight. We estimate that the front of the GOCE wing heats up to 70 °C, and the rear side remains around 50 °C. Scaling through the wing area leads to approximate values of heat capacitance of 6100J K<sup>-1</sup> and 2800J K<sup>-1</sup> for front and rear, respectively.

For the body-mounted panels, we follow a similar approach, with the operational modelled temperatures as described above. This leads to the thermal capacitances of 4300J K<sup>-1</sup> and 3800J K<sup>-1</sup> for larger and smaller panels, respectively.

The internal heat generated by the onboard electronics was adjusted to assure realistic operational temperature (25 °C). The internal heat generation has been set to 70W.

The details on calculating thermal resistance values for GOCE are provided in the next section.

# 3.2.2. Thermal resistance

Thermal resistance is a function of a fabric's thickness and thermal conductivity and determines the material's insulation properties. It can be defined as the ratio of the temperature difference between the two faces of a material to the rate of heat flow per unit area (Mishra et al., 2018).

Both the satellite wings and the body-mounted solar panels were thermally de-coupled from the platform by

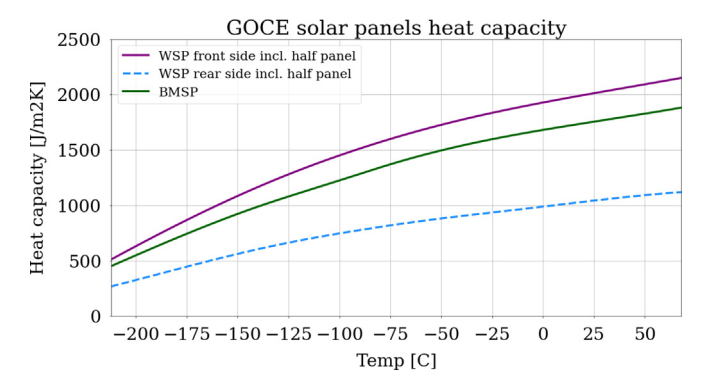


Fig. 5. Heat capacity of GOCE solar panels body-mounted solar panels (BMSP) and wing solar panels (WSP) as provided in the technical documentation (Dutch Space, 2006). Values for higher temperatures have been linearly interpolated.

titanium brackets and thermal washers (Cataloglu et al., 2004). Moreover, the MLI blankets were placed below the body-mounted panels for additional insulation (Battaglia et al., 2008). This assures high thermal resistance towards the satellite body.

To precisely model the heat flow through the wing wall, we use the information about the material layers provided in the documentation. In a composite structure such as the satellite wing, the total thermal resistance  $R_{total}$  can be calculated as a sum of the individual resistance of each layer by

$$R_{total} = \frac{1}{A} \sum_{j} R_j = \frac{1}{A} \frac{l_j}{k_j},\tag{15}$$

where  $l_j$  is a thickness of the layer,  $k_j$  is the conductivity and A area (Adhya, 2005).

Fig. 6 depicts the schematic cross-section of the GOCE solar panel comprising 11 materials based on the 'GOCE Solar Array: Detailed Thermal Model Analysis' document (Dutch Space, 2006).

Table 1 summarizes each layer's properties, considering the material type, thickness, and conductivity. Part of the information stems from Adhya (2005), who carried out a similar study to identify and describe the structure of a GPS Block IIR satellite.

Using the information from Table 1, the total resistance of the wing was calculated following Eq. 15 considering the panel areas. Note that the number of layers in the wing varies depending on whether the surface element is covered by solar cells or not. To distinguish between the area covered by the solar cells and that covered only by the adhesive, the thermal resistance was calculated for the whole panel surface and then scaled through the packing factor.

The total thermal resistance R of a panel is

$$R = R_{\text{cell}} + R_{\text{adhesive}} = \frac{1}{A_{\text{cell}}} \sum_{j=1}^{4} R_j + \frac{1}{A_{\text{adhesive}}} \sum_{j=5}^{12} R_j,$$
 (16)

where  $A_{\rm adhesive}$  is the area covered by adhesive (which corresponds to the total panel area of 2.828m), and  $A_{\rm cell}$  is the fraction of the surface covered by the solar cells (see packing factor, Section 3.2.1).

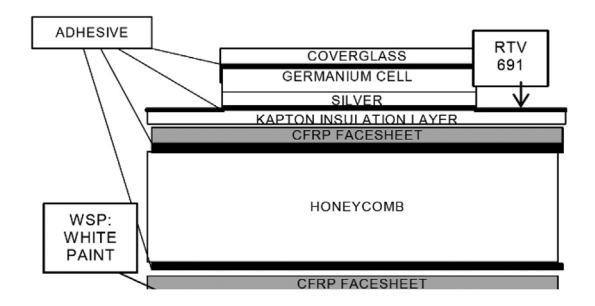


Fig. 6. The schematic cross-section of typical GOCE solar panel (Dutch Space, 2006).

Table 1 Material properties by layer. The thickness refers to the thickness of a single layer.

Layer [-]	Material [-]	Thickness [m]	Conductivity $[W m^{-1} K^{-1}]$	Layers [-]
1	Coverglass	$2.54 \times 10^{-4}$	1.417 <sup>2</sup>	1
2	Adhesive RTV	$1.02 \times 10^{-4}$	$0.157^{2}$	1
3	Germanium cell	$2.30 \times 10^{-4}$	$41.0^{1}$	1
4	Silver	$1.00 \times 10^{-4}$	419 <sup>1</sup>	1
5	Adhesive RTV	$1.02 \times 10^{-4}$	$0.157^{2}$	1
6	Kapton insulator	$2.54 \times 10^{-5}$	$0.157^{2}$	1
7	CFRP	0.001	$0.35^{1}$	5
8	Adhesive RTV	$1.02 \times 10^{-4}$	$0.157^{2}$	1
9	Honeycomb	$6.52 \times 10^{-2}$	$2.03^{2}$	1
10	Adhesive RTV	$1.02 \times 10^{-4}$	$0.157^{2}$	1
11	CFRP	0.001	$0.35^{1}$	5
12	White paint	$1.00 \times 10^{-4}$	$0.2^{1}$	1

<sup>&</sup>lt;sup>1</sup> Material Property Data:https://www.matweb.com/, accessed on 20/08/2024.

From Table 1, we deduced  $R_{\rm cell} = 0.00042~{\rm W\,K^{-1}}$  and  $R_{\rm adhesive} = 0.01469~{\rm W\,K^{-1}}$ . Therefore, the total thermal resistance of a GOCE wing amounts to  $R = 0.01469~{\rm W\,K^{-1}}$ . For the wing solar panels, for which the information about the layers is available, we can calculate the thermal resistance. Moreover, we have the rear-side thermistor measurement available to verify the temperatures resulting from these resistance values. As for the body-mounted panels, they remain very well insulated from the interior, assuring the operational internal temperature of approximately 25 C. We used this criterion to calculate the thermal resistance instead of relying on layers.

#### 4. Results and discussion

# 4.1. Solar radiation pressure modelling

In this work, we distinguish between the two frequency bands of the solar spectrum: visible and infrared (see Section 3.1). Typically, the total solar flux is approximated by integrating over all wavelengths and assuming that interactions occur only at the visible wavelength (i.e., only the visible surface properties are used in combination with the total solar flux). In our approach, we select the appropriate surface coefficients based on the specific wavelength, using either visible or infrared properties. Fig. 7 illustrates an example of two satellites, GOCE and Gravity Recovery and Climate Experiment Follow-On (GRACE-FO), showing the differences in solar radiation pressure (SRP) acceleration when the flux is split by wavelength or integrated. For both satellites, splitting the solar flux increases the radiation pressure estimate in the cross-track direction. The differences, reaching up to 4nm s<sup>-2</sup> for GOCE and 3nm s<sup>-2</sup> for GRACE-FO, directly impact the crosswind estimation. On the other hand, the along-track acceleration

<sup>&</sup>lt;sup>2</sup> (Adhya, 2005).

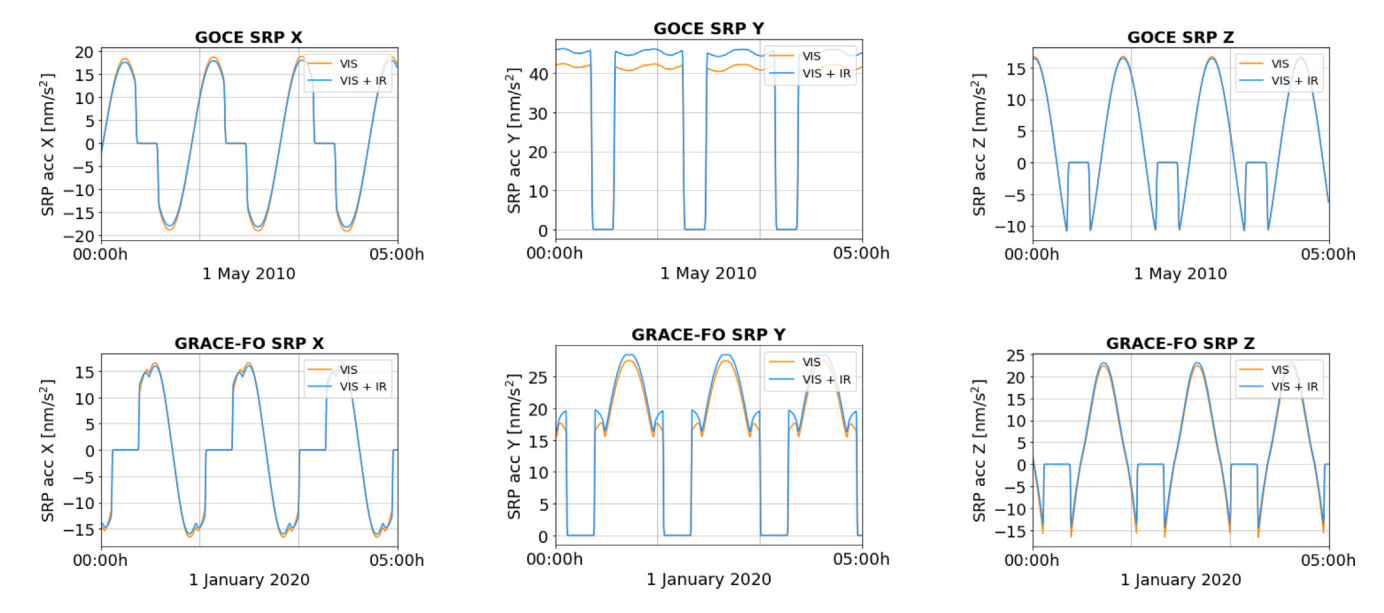


Fig. 7. Solar radiation pressure acceleration (SRP) in along-track, cross-track and radial directions calculated using integrated (orange) and solar flux split by wavelength (blue). The top and bottom rows show examples from the GOCE and GRACE-FO satellites, respectively.

decreases by approximately  $1 \text{nm s}^{-2}$  for both satellites when the split flux is used. The changes are negligible in the radial direction. This pattern may vary depending on the satellite, its surface properties and orbital characteristics.

To our knowledge, no publicly available document provides official information on GOCE's thermo-optical surface properties. Therefore, the ray-tracing model was based on the information about satellite materials available in the satellite thermal control documentation (Valentini et al., 2006; Battaglia et al., 2008) and the information on the thermo-optical properties of the specific materials used

for the satellite design (Fortescue et al., 2011; Silverman, 1995). The satellite surface properties used in the ray-tracing simulation are summarized in Table 2. To model the eclipse in this work, we utilize the Solar radiation pressure with Oblateness and Lower Atmospheric Absorption, Refraction, and Scattering Curve Fit (SOLAARS-CF) model (Robertson et al., 2015).

# 4.2. Thermal emission

The crosswind data are sensitive to acceleration modelling errors in the y-direction. Moreover, the thermal emis-

Table 2
GOCE thermo-optical surface coefficients for visible and infrared light. The visual representation of the Sun-facing panels has been shown in Fig. 1.

Panel	$A_j$	$n_{x,j}$	$n_{y,j}$	$n_{z,j}$	$c_{{ m vis},a,j}$	$c_{\mathrm{vis},d,j}$	$c_{{ m vis},s,j}$	$c_{{ m ir},a,j}$	$c_{{ m ir},d,j}$	$c_{{ m ir},s,j}$
	$[m^2]$	[-]	[-]	[-]	[-]	[-]	[-]	[-]	[-]	[-]
Front	0.865	1.000	0.000	0.000	0.07	0.23	0.70	0.74	0.20	0.06
Rear	0.865	-1.000	0.000	0.000	0.10	0.05	0.85	0.80	0.15	0.05
			S	un-facing side	(solar panels)					
Body 1	2.067	0.000	-0.924	-0.383	0.95	0.05	0.00	0.60	0.29	0.11
Body 2	1.918	0.000	-0.383	-0.924	0.95	0.05	0.00	0.60	0.29	0.11
Body 3	1.918	0.000	-0.383	0.924	0.95	0.05	0.00	0.60	0.29	0.11
Body 4	2.067	0.000	-0.924	0.383	0.95	0.05	0.00	0.60	0.29	0.11
Wing 1/2	2.828	0.000	-1.000	0.000	0.95	0.05	0.00	0.60	0.29	0.11
				Sun-oppos	site side					
Body 1	1.874	0.000	0.383	-0.924	0.15	0.35	0.50	0.05	0.25	0.70
Body 2	1.601	0.000	0.924	-0.383	0.15	0.35	0.50	0.05	0.25	0.70
Body 3	1.601	0.000	0.924	0.383	0.15	0.35	0.50	0.05	0.25	0.70
Body 4	1.874	0.000	0.383	0.924	0.15	0.35	0.50	0.05	0.25	0.70
Wing 1/2	2.828	0.000	1.000	0.000	0.35	0.55	0.10	0.75	0.20	0.05
				Radiat	tors					
Radiator Front	0.036	1.000	0.000	0.000	0.10	0.20	0.70	0.80	0.15	0.05
Radiator Rear	0.036	-1.000	0.000	0.000	0.10	0.20	0.70	0.80	0.15	0.05
Radiator 1	0.101	-0.924	0.383	0.101	0.10	0.20	0.70	0.80	0.15	0.05
Radiator 2	0.061	-0.383	-0.924	0.061	0.10	0.20	0.70	0.80	0.15	0.05

sion is proportional to the temperature raised to the fourth power (Eq. 8), meaning that the panels with higher temperatures exert greater thermal acceleration. Thus, in this work, we focus specifically on modelling the temperature of the solar arrays, which were on the Sun-facing side of the satellite and, therefore, reached much hotter temperatures than the panels on the Sun-opposing side.

Fig. 8 gives an overview of the modelled and measured temperatures of all solar arrays during the timespan of a few orbits. The measured temperatures were calculated as the average value between two thermistors located on the same panel. It is important to note that the thermistors serve only as a rough reference for our thermal modelling, and direct comparison is not possible. Since the thermistors were mounted on the rear side of the panels, they were shielded from direct sunlight. Consequently, the measured temperatures exhibit smaller variations compared to the modelled ones, while displaying a similar pattern. The body-mounted inner panels (Fig. 8a, Fig. 8d) reach the highest temperatures because they have the smallest incidence angle to the incoming radiation from the Sun. In contrast, the temperature is lower for the upward- and downward-facing outer panels (Fig. 8b, Fig. 8e). As shown here, during the summer the Earth-opposed panels get hotter than the Earth-facing panels due to the tilt of the orbital plane with respect to the Sun. Figs. 8c and 8f present the temperature model for both the front and rear sides of the wing. As anticipated, the modelled orbit mean temperatures are higher than those recorded by the thermistors, with the exception of the Earth-facing panel (Fig. 8e), where the modelled and measured temperatures are of similar magnitude. This could be attributed to errors in the thermistor's measurements or inaccuracies in Earth's albedo and infrared radiation modelling.

The results of the thermal modelling for the GOCE wing are shown in Fig. 9. In this work, we use the argument of latitude to illustrate the position of the satellite along the orbit. The horizontal axis of the figure refers to time, and the vertical axis refers to the argument of latitude. Argument of latitudes of 0° and 180° refer to the ascending and descending equator crossings, while 90° and 270° represent the northern and southernmost points of the orbit, respectively.

As expected, the modelled temperature of the front side of the wing (Fig. 9a, 9b), which is facing the Sun, exhibits a higher value compared to the rear side (Fig. 9c, 9d). Since the panel geometry used for thermal modelling does not account for shadowing, the modelled temperature of the front and rear sides is symmetrical for both Earth-facing and Earth-opposed wings. Fig. 9e shows the average measured temperature of two thermistors on Earth-facing wing, and Fig. 9f shows the same for the Earth-opposed wing. Fig. 9g and 9h shows the difference between the measured and modelled temperatures. For the Earth-facing wing, the temperature differences in sunlight are approximate 3 °C, and in the shadow, they remain within 15 °C. In case of the Earth-opposed wing the differences are respectively 7 °C and 20 °C. This indicates that the difference between the modelled and measured temperature has the same magnitude as the differences between measurements of the thermistors located on the same wing (Section 2.2).

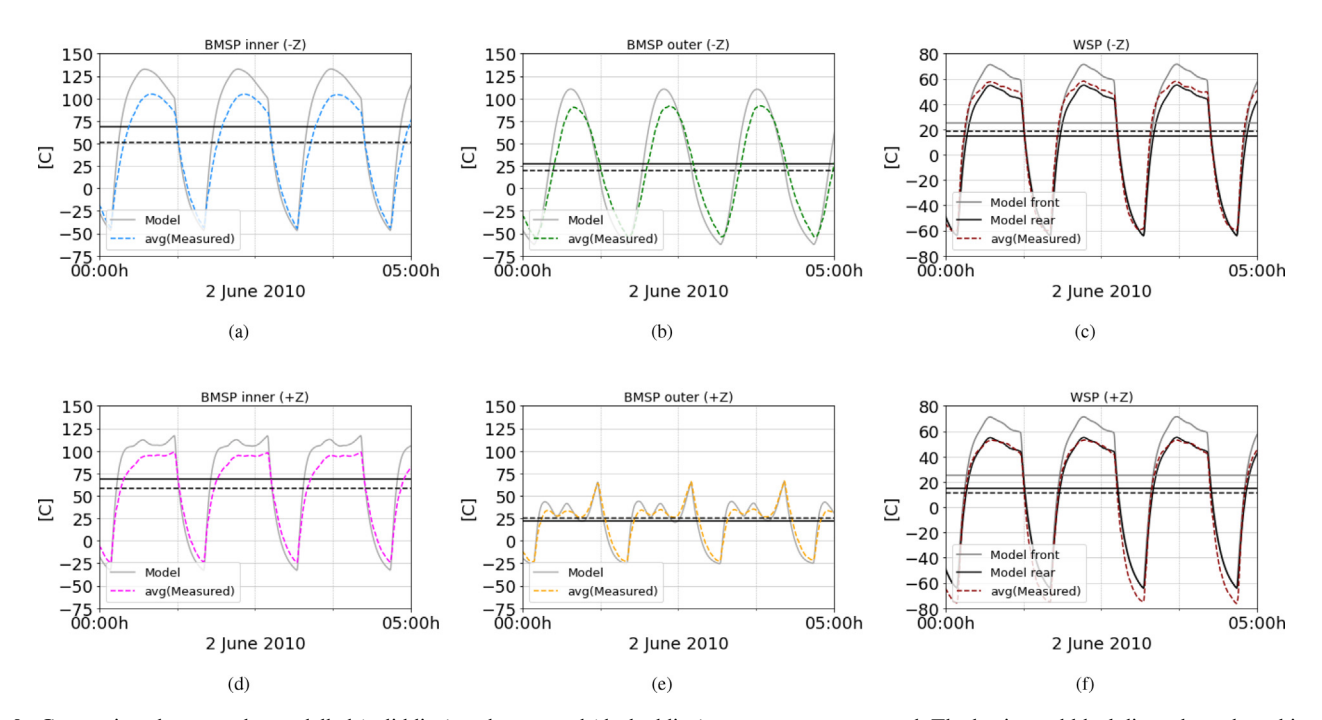


Fig. 8. Comparison between the modelled (solid line) and measured (dashed line) temperatures per panel. The horizontal black lines show the orbit mean temperature of the model (solid) and measurements (dashed). The panels presented in the top row are Earth-opposed, while the panels in the bottom row are Earth-facing.

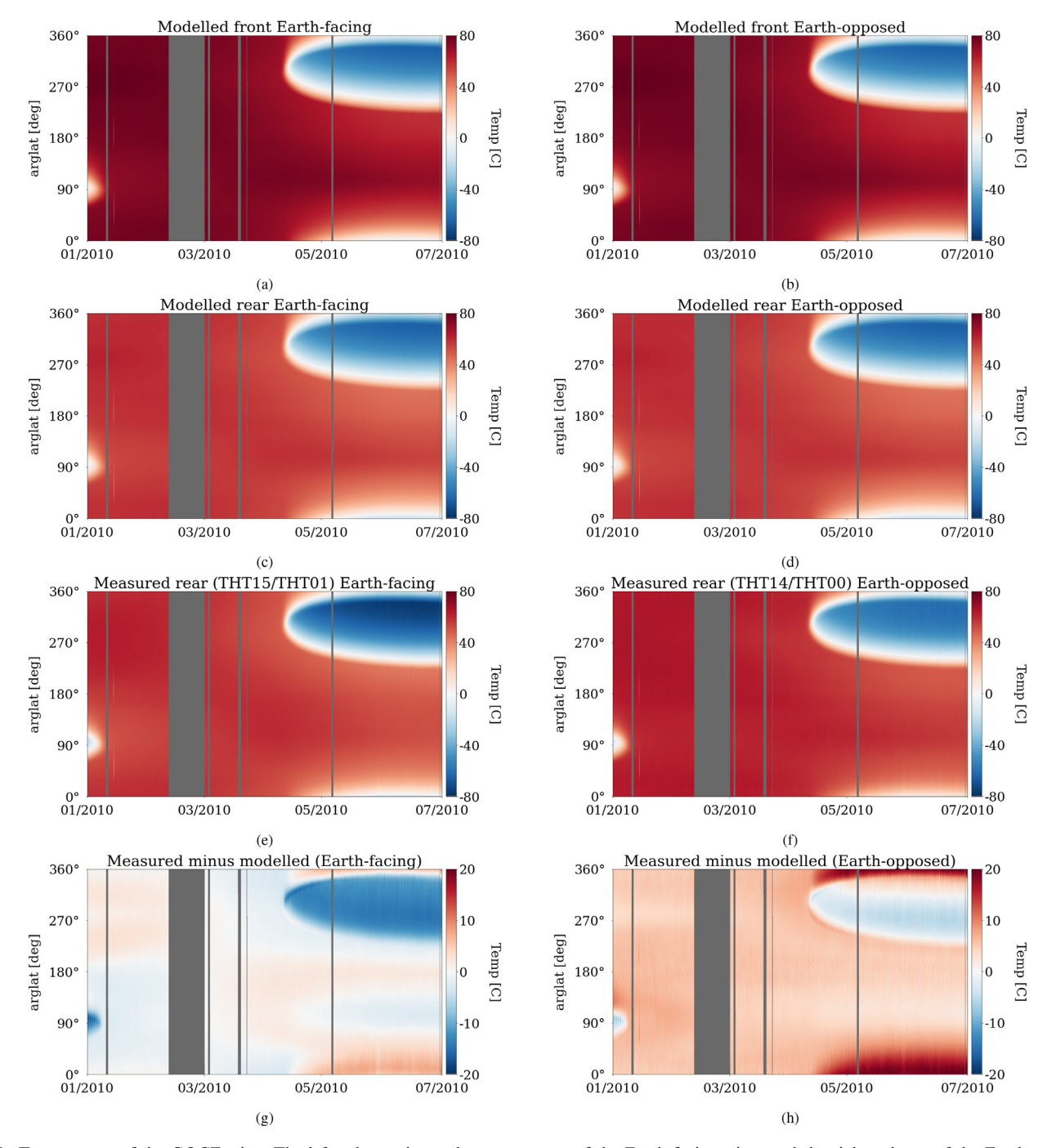


Fig. 9. Temperature of the GOCE wing. The left column shows the temperature of the Earth-facing wing, and the right column of the Earth-opposed wing. The first and second rows depict the front and rear modelled temperatures, respectively. The third row shows the average measured temperature by the THT14/THT01 thermistors (e) and THT15/THT00 thermistors (f). The last row shows the difference between the measured temperatures and modelled ones.

Table 3 summarizes the material properties used for thermal modelling. Only the geometry elements which contribute primarily to the total thermal emission were summarized in the table. The remaining elements, such as the stabilizer, contribute less than  $0.5 \, \text{nm/s}^2$  to the total crosstrack thermal acceleration and, therefore, were not listed. It should be mentioned that in our model, we assume that the panel is heated evenly.

# 4.3. Horizontal crosswind and density

The low operational altitude of GOCE, which led to high aerodynamic accelerations, provided an advantage for obtaining valuable crosswind data. The newly produced GOCE neutral thermosphere density (Fig. 10) and horizontal wind datasets (Fig. 11) labelled as Version V02 are available on the TU Delft Thermosphere FTP Server.

Table 3 GOCE thermal radiation model. The internal heat generation has been set to 70 W. It should be noted that the panel thermal capacitance is inversely proportional to the resistance  $k_j = R_j^{-1}$ . The value of areas and panel's normals are identical to the ones presented in Table 2.

Panel	$C_i$	$k_i$	$e_i$
	$[J K^{-1}]$	$[\mathbf{W}\mathbf{K}^{-1}]$	[-]
Front	4000	0.1	-
Rear	9000	0.1	-
	Sun-facing side (sol	ar panels)	
Body 1	4300	0.1	0.10
Body 2	3800	0.1	0.11
Body 3	3800	0.1	0.11
Body 4	4300	0.1	0.10
Wing 1/2	6100	68.9	0.15
	Sun-opposite	side	
Body 1	2000	0.1	-
Body 2	2000	0.1	-
Body 3	2000	0.1	-
Body 4	2000	0.1	-
Wing 1/2	2800	68.9	-
	Radiators		
Radiator Front	400	0.1	-
Radiator Rear	400	0.1	-
Radiator 1	400	0.1	-
Radiator 2	400	0.1	_

These datasets incorporate the advancements in SRP modelling, including splitting the solar flux into the visible and infrared bands, using the ray-tracing algorithm in combination with the high-fidelity satellite geometry, and updating the thermo-optical surface coefficients. It also includes the thermal satellite model to account for the acceleration due to the satellite's thermal emission.

Fig. 12 quantifies the impact of the advances on the horizontal winds by incrementally introducing additional features in the radiation pressure model, as indicated in Table 4. In the simplest case (a), the satellite geometry is represented by a panel geometry, the satellite's thermal emissions are not modelled, and solar radiation pressure is obtained from the flux integrated over the whole spectrum in combination with surface coefficients for visible light. Then, we introduce the high-fidelity geometry in case (b), the thermal model in case (c), and distinguish between visible and infrared wavelengths of the solar flux in case (d). To highlight the impact of each modelling feature, we show the difference between cases (a) and (b), and (c) and (d). For the comparison, we selected the time interval from 2010 to 2013, aligning with the satellite's operational phase while avoiding periods with too many manoeuvres.

For all three panels of Fig. 12, the biggest differences appeared in 2010, when the solar activity was lowest and, consequently, the aerodynamic acceleration making changes in the radiation pressure acceleration more noticeable. By replacing the panel model with the high-fidelity geometry (Fig. 12.1), the estimated horizontal wind speed decreased by approximately 5ms<sup>-1</sup>. The largest decrease of up to 40ms<sup>-1</sup> resulted from introducing the thermal model (Fig. 12.2). In this case, the satellite emitted infrared

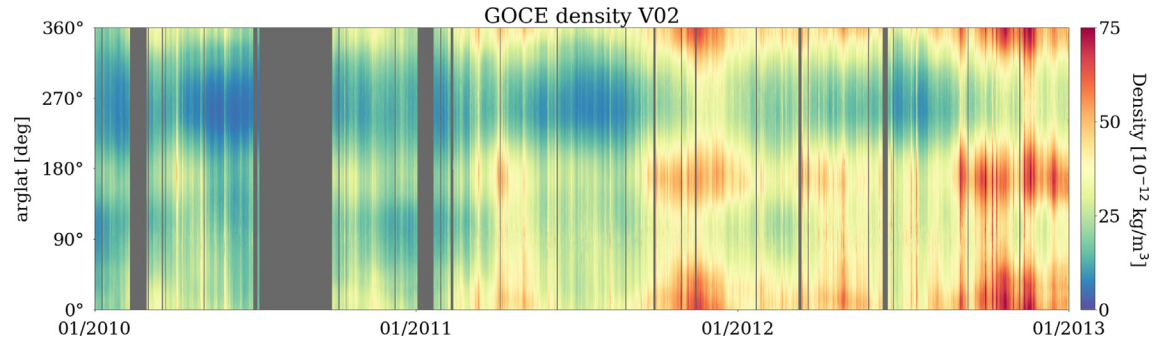


Fig. 10. Version V02 of the GOCE neutral thermosphere mass density.

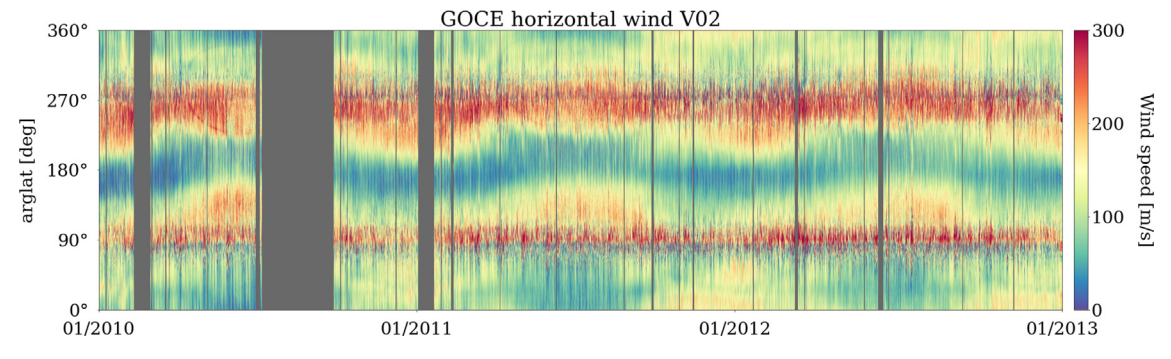


Fig. 11. Version V02 of the GOCE horizontal windspeed.

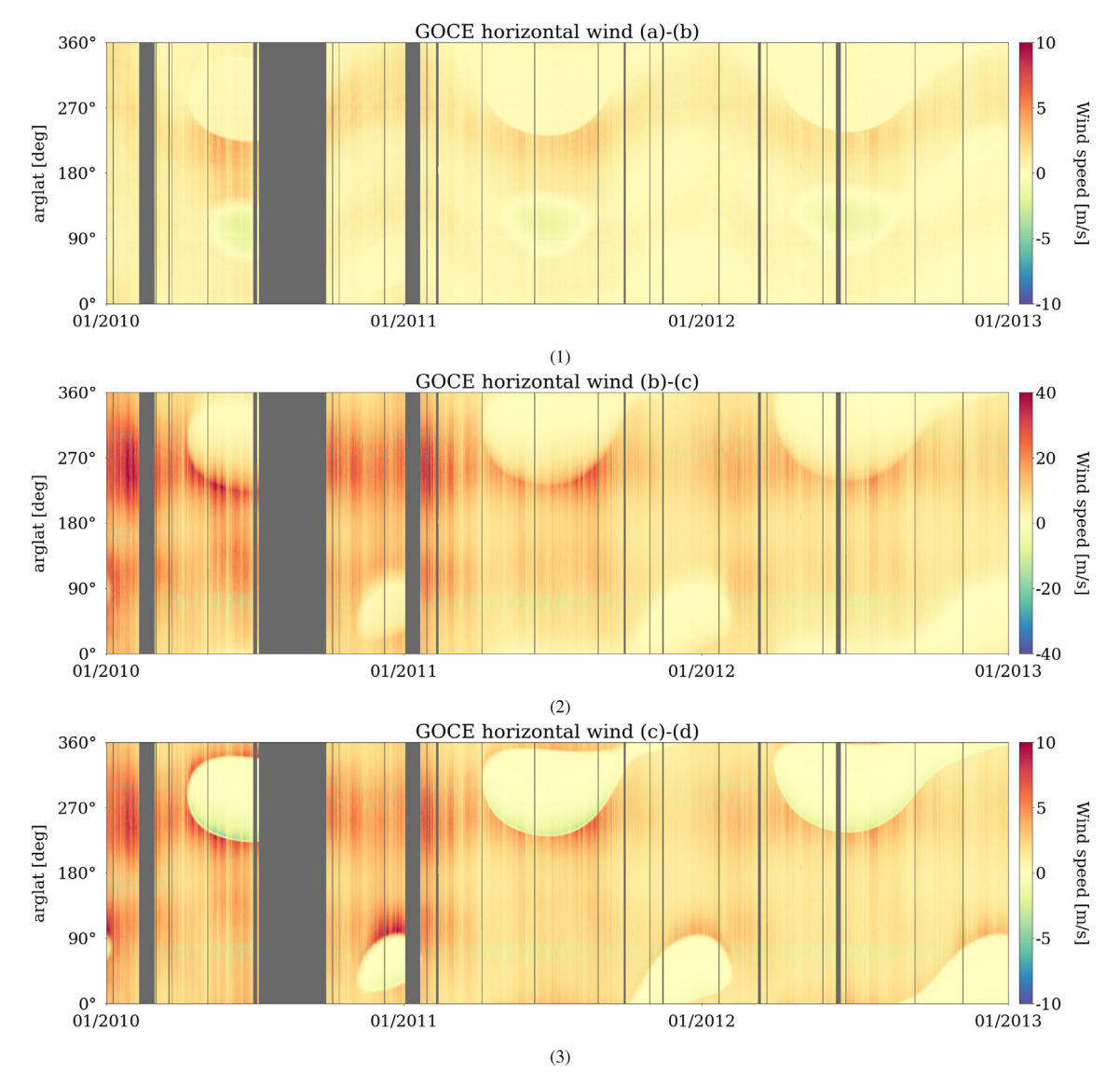


Fig. 12. Quantification of the advancements in the radiation pressure modelling as described in Table 4. The difference in the scale of the colour bars should be noted.

Table 4
The summary of GOCE radiation pressure modelling approaches.

Case	Thermal model included	Geometry model	Solar flux split by wavelength
(a)	no	panel	no
(b)	no	high-fidelity	no
(c)	yes	high-fidelity	no
(d)	yes	high-fidelity	yes

radiation due to its nonzero absolute temperature. As the satellite heated up in the sunlit part of the orbit due to absorbed solar radiation, the resulting thermal emission acceleration caused changes in the estimated wind. The changes in the estimated wind shortly after the satellite entered the eclipse can be explained by the fact that it took several minutes before the satellite cooled down so much

that the thermal emission acceleration became insignificant (for eclipses, see Fig. 13). Finally, splitting the solar flux by wavelength further reduced the estimated wind by up to 8ms<sup>-1</sup> (Fig. 12.3).

The previous version of the GOCE crosswind dataset is labelled version V01 in TU Delft's thermosphere database and version 2.0 in ESA's GOCE data collections website (despite the different versions, it is the same dataset). In this work, we will refer to the newly produced dataset as V02 and the previously produced dataset as V01, following the convention in the TU Delft's thermosphere database.

The version V01 dataset provides both the thermosphere neutral density and crosswind estimates. The crosswind data was generated using a method described by Visser et al. (2019). The method utilises the concept of simultaneous observation of linear and angular accelerations, so the derived winds rely on both forces and torque modelling.

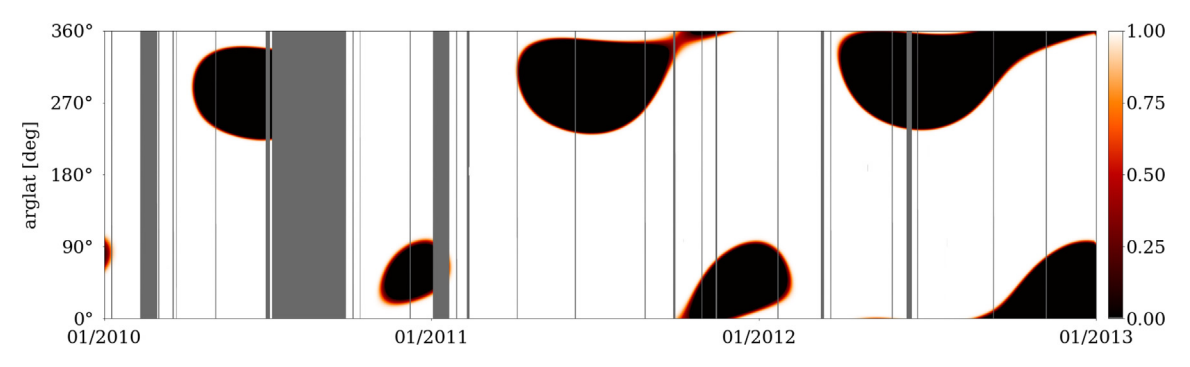
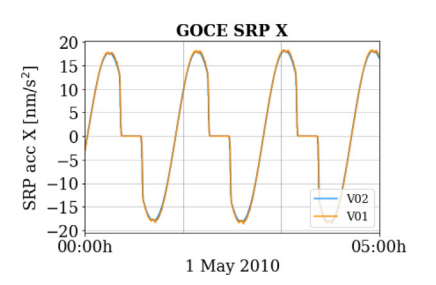
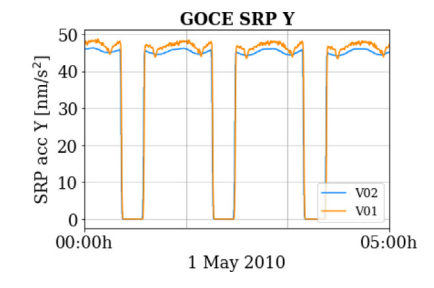


Fig. 13. GOCE shadow function.





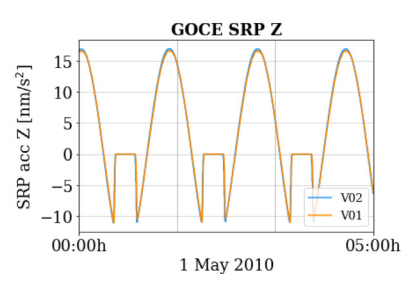


Fig. 14. The comparison between the SRP acceleration used in Version V01 and V02. It should be noted that the V01 wind dataset also relies on the SRP torques in addition to the linear accelerations.

Visser et al. (2019) used the high-fidelity satellite geometry model (Section 2.3) for aerodynamic modelling, assuming diffuse reflections of gas particles with incomplete energy accommodation of  $\alpha_E = 0.82$  (March et al., 2019a). They used a simplified solar radiation pressure model, assuming a reflectance of zero for the side covered by solar panels and 0.8 for the other side. For modelling of albedo and Earth's infrared radiation, they utilized the monthly mean top-of-atmosphere albedo and infrared flux maps obtained from the CERES SYN1deg product<sup>1</sup>. The eclipse was defined by the physics-based SOLAARS-CF model (Robertson et al., 2015).

To produce version V02, we retrieved the crosswind estimates with the iterative algorithm proposed by Doornbos et al. (2010), which relies solely on the satellite linear accelerations. The intrinsic differences between the methods of Doornbos et al. (2010) and Visser et al. (2019) may lead to discrepancies in crosswind estimates, making the interpretation of the differences challenging. Nevertheless, version V01 can still serve as a valuable reference for comparison between the two datasets.

Since interpreting the crosswind comparison between versions V01 and V02 directly can be challenging, we first compare only the results of the solar radiation pressure modelling. Fig. 14 shows the SRP acceleration used in V01 and V02. There is a good agreement between both versions, regardless of V01 using the simple panel model and

limited knowledge of the thermo-optical properties of materials. The difference between V01 and V02 is 3nm  $\rm s^{-2}$  in the cross-track direction and smaller than 1nm  $\rm s^{-2}$  in the along-track and radial directions.

Fig. 15.a shows the difference in the crosswinds between the newly produced version V02 and the version V01. At the beginning of the mission, version V02 winds have a lower magnitude in comparison to V01, evident from negative differences. Considering the difference in the SRP magnitude between both versions (Fig. 14), the decrease of the wind in the first year is likely due to the introduction of the thermal emission acceleration. We interpret this as an improvement, assuming that smaller crosswinds are likely more accurate. As the density increases over time (Fig. 15.c), the wind difference changes sign, meaning that V01 crosswinds have a smaller magnitude than V02. This could be attributed to errors in the aerodynamic modelling (manifesting at higher densities) as well as differences between the algorithms used to produce both versions. Therefore, the wind retrieval algorithm used to generate V01 (Visser et al., 2019) should be revised and updated to incorporate recent improvements.

While the wind retrieval algorithm relies on the cross-track acceleration, the thermosphere density is derived from the along-track aerodynamic acceleration (Eq. 2). The ratio of radiative forces to the aerodynamic force in the along-track direction is much smaller than in the cross-track direction (see Fig. 3). Therefore, the improvement in the radiation pressure modelling is best reflected in the crosswind rather than in the density. Fig. 15.b shows the relative density difference towards V01. The

https://ceres.larc.nasa.gov/data/#synoptic-toa-and-surface-fluxes-and-clouds-syn, accessed on 20/05/2025.

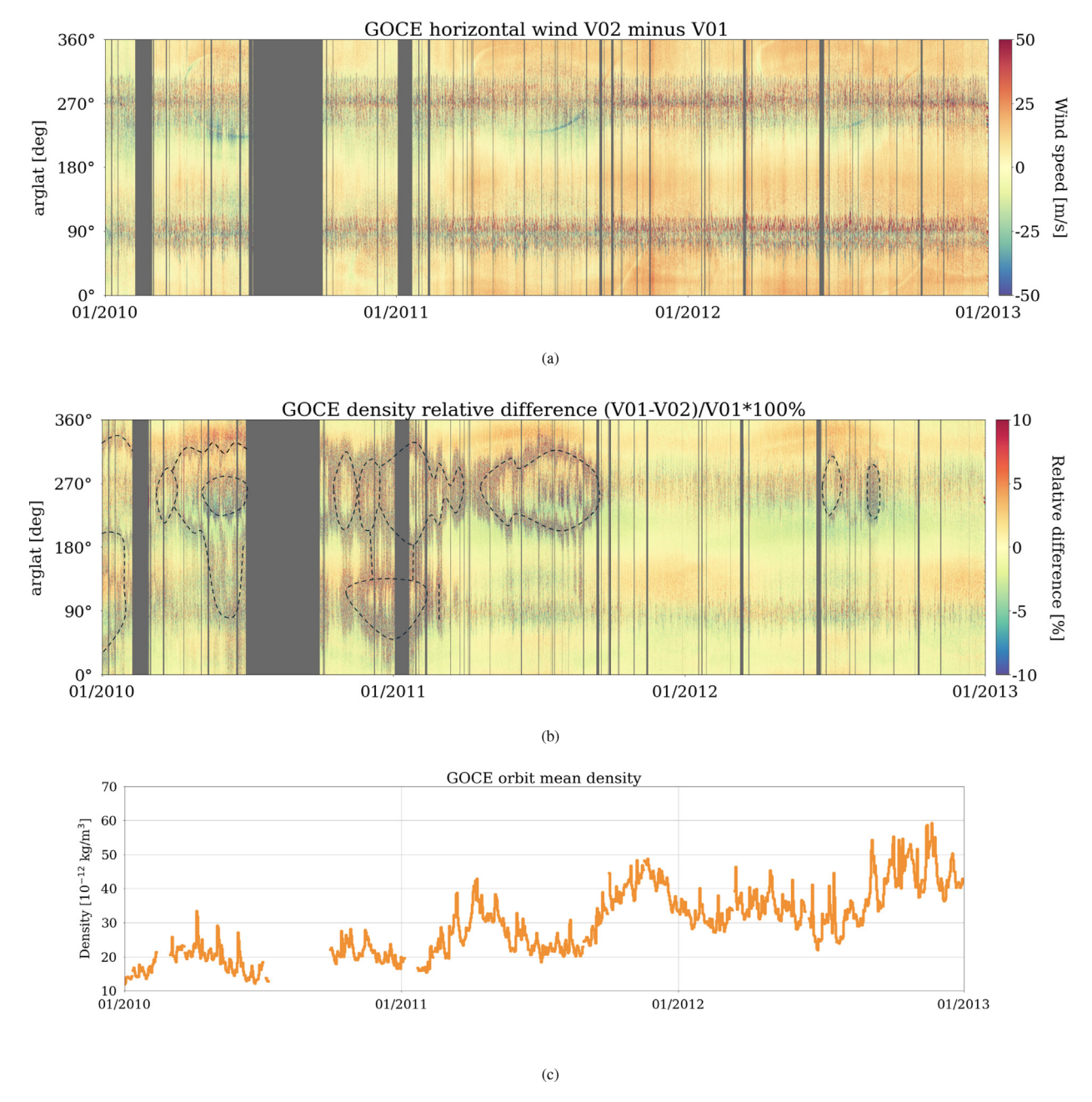


Fig. 15. Evolution of the GOCE orbit mean density and the differences between versions V01 and V02 of the neutral thermosphere density and horizontal wind.

overall differences are very small, with the biggest impact (up to 7%) visible around the eclipse regions during 2010/2011 when the solar activity was low. The features highlighted by dashed lines are caused by high-frequency thrust noise, a real acceleration signal. Since the L1b thruster data has a lower sampling rate than the raw telemetry, the feature is either smoothed out or aliased in the former (the details of the L1b thruster data processing are unknown to us). Hence, it appears as high-frequency noise in the density difference. The new GOCE dataset includes a flag indicating when density data is affected by thruster noise.

Finally, since a comparison of the GOCE densities to other datasets is out of the scope of this paper, we refer to Bruinsma (2014) for such a comparison.

The thermospheric wind pattern depends, among others, on the season of the year, local solar time, and geomagnetic conditions (Wang et al., 2021). Due to a very small orbital precession, GOCE's local time remained roughly fixed throughout the mission. The ascending equatorial crossing of the satellite drifted from 18:00 local time at the beginning of the mission to 19:30 local time at the end (Bock et al., 2014). This orbital characteristic provided a perfect opportunity to study seasonal and annual variations in

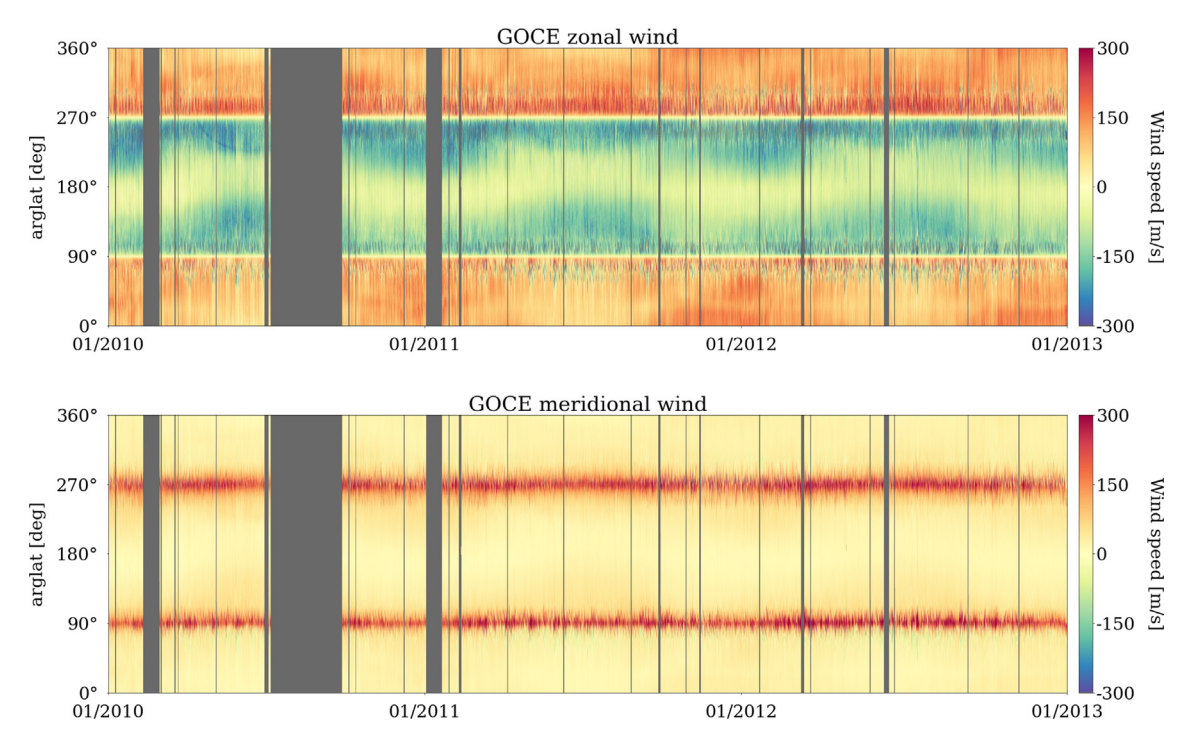


Fig. 16. Distinction between GOCE zonal and meridional winds V02. The seasonal wind pattern repeating through the year is clearly visible in the zonal winds.

the wind data. As a result of its near-polar orbit, the winds are closely aligned with the zonal direction at low and midlatitudes and with the meridional direction at the poles, which is illustrated in Fig. 16. The seasonal dependency is clearly visible in the zonal winds, with a cyclical pattern that repeats throughout the mission.

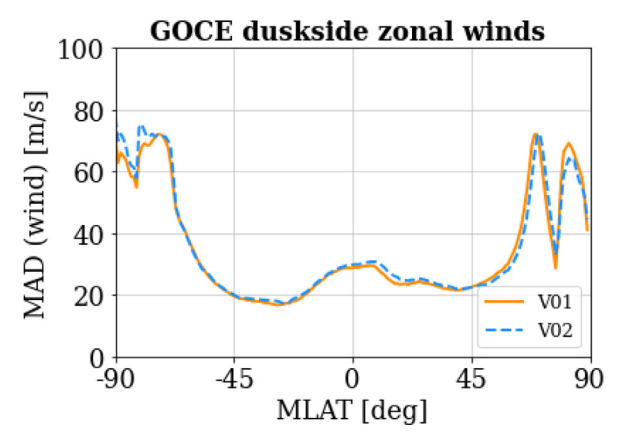
The study performed by Dhadly et al. (2017) and Dhadly et al. (2018) showed that there is an offset between the accelerometer-derived GOCE zonal wind data and the models. The study compared the GOCE data with various ground-based and space-based datasets, including Fabry-Perot interferometers, Scanning Doppler imaging Fabry-Perot interferometers, as well as space-based instruments flying on the Upper Atmosphere Research Satellite and Dynamic Explorer 2. The study concluded that amongst all these datasets, the GOCE in situ crosswind data have been overestimated, with the differences. This offset increases with latitude and is particularly noticeable on the duskside. It should be noted that the authors' comparison did not yet include Version V01 but relied on an even older version of the dataset. Nevertheless, we can use this information to quantify the improvement in the new wind data.

To verify this assumption, we divided the zonal wind data in the dusk and dawn sectors and binned with a resolution of  $1^{\circ}$  magnetic latitude (MLAT). Then we calculated the median absolute deviation (MAD) of each bin. Fig. 17 shows the comparison between the V01 and V02 data. At low latitudes, the wind distribution is similar for both versions in both the dusk and dawn sectors. In the South Pole region (approximately  $-80^{\circ}$  to  $-70^{\circ}$  MLAT), there is a

decrease of wind MAD of approximately 10ms<sup>-1</sup> for the dawn sector. Around the North Pole (70°–80° MLAT), the MAD decreases on the dusk side, but it slightly increases on the dawn side. These variations in MAD may be linked to eclipse transitions occurring at these latitudes, which are affected by the updated thermal emission modeling.

We can also assess the data quality by checking the consistency of zonal wind data. To do so, first, we divided the dataset into three yearly bins: 2010, 2011 and 2012. In the next step, we split the data into the dusk and dawn sectors and limited it to the low latitudes (argument of latitudes  $0^{\circ} \pm 45^{\circ}$  and  $180^{\circ} \pm 45^{\circ}$ ) to prevent the complex wind dynamics at the poles from affecting the statistics. To calculate data consistency, we subtracted the wind from the consecutive years and calculated the MAD. Table 5 shows the MAD comparison between Version V01 and V02. The wind consistency is similar between both versions, with a slight enhancement of V02 in the dawn sector, especially for the 2010-2011 bin. This indicates that even though the magnitude of the total wind speed differs between both versions (Fig. 15.a), the consistency between the zonal component of the low-latitude winds is similar.

To produce the Version V02 dataset, we used the energy accommodation coefficient of 0.82. This is in line with the study by March et al. (2019b), who optimised the gassurface interaction DRIA (Diffuse Reflection Incomplete Accommodation) model by investigating the consistency of the GOCE winds. After implementing the radiation pressure improvements, we verified whether this assumption was still valid.



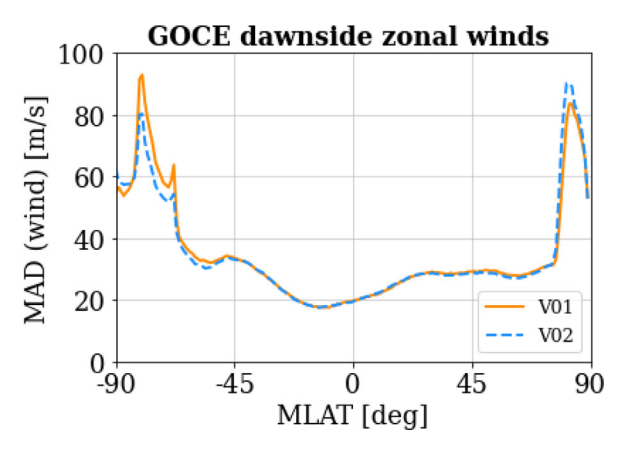


Fig. 17. Median absolute deviation (MAD) of GOCE zonal winds with 1° MLAT binning.

Table 5 Comparison between Version v01 nad v02 wind consistency.

Years	Time	V01 MAD [m/s]	V02 MAD [m/s]
2010–2011	Dawn	25.20	24.72
	Dusk	24.02	23.92
2011-2012	Dawn	20.51	20.25
	Dusk	20.67	20.66

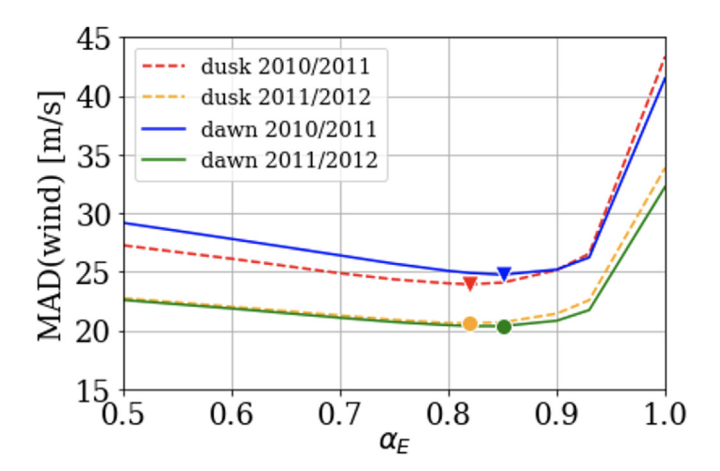


Fig. 18. Median absolute deviation of the Version v02 GOCE zonal wind, restricted to the argument of latitude  $0^{\circ} \pm 45^{\circ}$  and  $180^{\circ} \pm 45^{\circ}$ , as a function of energy accommodation coefficient.

Fig. 18 shows the zonal component of GOCE wind data produced for the energy accommodation coefficients ranging between 0.5 and 1.0. We followed a similar approach as explained in the previous analysis, starting by arranging the dataset into three yearly bins. By dividing the data into years instead of seasons (as proposed by March et al. (2019b)), we captured the seasonal wind variations while mitigating the effect of prolonged data gaps (such as the one occurring in July 2010). Likewise, in the previous analysis, we restricted the data selection to low-latitude and divided it into dawn and dusk sectors. To calculate the data consistency, we subtracted the wind from the consecutive

years and calculated MAD. The markers pinpoint the minimum MAD for each curve. The optimum energy accommodation coefficients are  $\alpha_E = 0.82$  and  $\alpha_E = 0.85$  for the dusk and dawn sectors, respectively, with the best estimate for the energy accommodation coefficient lying between these values. Therefore, we conclude that introducing the new radiation pressure model did not notably change the assumptions on the energy accommodation coefficient.

# 5. Summary and outlook

The aim of this study was to revisit and reprocess the GOCE horizontal wind data using enhanced force modelling standards. The key improvement was the introduction of the thermal emission acceleration, which has never been accounted for in the previous GOCE datasets. Moreover, this study has advanced the solar radiation pressure modelling, including updating the thermo-optical surface coefficients and using a ray-tracing method. We collected and presented information on the GOCE surface materials relevant for radiation pressure modelling, including the GOCE panel model, from multiple sources. The information on the surface materials can be readily reused in the context of other missions. For a more realistic model, the solar flux was split between two wavelengths: visible and infrared. The ion thruster Level-1b data were replaced by raw telemetry filling multiple data gaps. Furthermore, this research served as an opportunity to compare the new dataset with the previously published one, evaluating wind consistency and magnitude, as well as verifying the assumptions about the energy accommodation coefficient.

We took advantage of thermistor data located on the Sun-opposed side of the satellite wing to realistically model the heat transfer and the wing surface temperature. However, since the other thermistors were placed on the rear side of the panels, a direct evaluation of surface temperature was not possible. Similar limitation was encountered for the GRACE mission (Hładczuk et al., 2024). Therefore, it would be beneficial from the perspective of thermal modelling to equip future missions with thermistors placed on

the top of the panels and distributed externally in multiple places.

Modelling the wavelength-dependent solar flux interaction with the satellite requires detailed knowledge of the material properties. Due to GOCE's low orbit, the degradation caused by the atomic oxygen results in erosion of the coating materials (Battaglia et al., 2008). Moreover, the surface properties of the satellites are affected by factors such as UV radiation exposure (Silverman, 1995). Addressing these factors would require an extensive study with a focus on laboratory testing. Therefore, some assumptions had to be made to ensure a compromise between model accuracy and simplicity. While accounting for the infrared part of the solar spectrum is crucial for applications which require precise force modelling, other missions with limited knowledge of surface properties may not significantly benefit from this distinction.

The solar flux varies not only in wavelength but also in magnitude. However, these variations are relatively minor. In this study, we did not account for the temporal variations in solar flux, which could be a point for future analysis. Future studies would also benefit from introducing Clouds and Earth's Radiant Energy System (CERES) data to improve vertical wind estimate as well as wind uncertainty quantification, similar to the one available for the density data (Siemes et al., 2024). Both of these aspects will be addressed in our future work.

# **Declaration of Competing Interest**

The authors declare that they have no known competing financial interests or personal relationships that could have appeared to influence the work reported in this paper.

### Acknowledgments

The authors would like to thank AIRBUS GmbH, and specifically Hauke Thamm, for kindly sharing the 'GOCE Solar Array: Detailed Thermal Model Analysis' document. We also extend our thanks to Tim Visser for sharing data and offering valuable insights on GOCE wind version V01.

#### References

- Adhya, S., 2005. Thermal Re-Radiation Modelling for the Precise Prediction and Determination of Spacecraft Orbits. PhD thesis. Department of Geomatic Engineering, University College London.
- Andreis, D., Canuto, E.S., 2005. Drag-free and attitude control for the goce satellite. In: Proceedings of the 44th IEEE Conference on Decision and Control. IEEE, pp. 3851–3856. https://doi.org/10.1109/ CDC.2005.1582794.
- Battaglia, D., Cataloglu, A., Dolce, S., 2008. GOCE thermal balance/vacuum test. Technical Report 2008–01-2034 SAE. International. https://doi.org/10.4271/2008-01-2034.
- Bruinsma, S., 2014. The DTM-2013 thermosphere model. Journal of Space Weather and Space Climate, 5, EDP Sciences. doi:10.1051/swsc/ 2015001.
- Bhattarai, S., Ziebart, M., Springer, T., et al., 2022. High-precision physics-based radiation force models for the Galileo spacecraft. Adv.

- Space Res. 69 (12), 4141–4154. https://doi.org/10.1016/j.asr.2022.04.003.
- Bock, H., Jäggi, A., Beutler, G., et al., 2014. GOCE: precise orbit determination for the entire mission. J. Geodesy 88 (11), 1047–1060. https://doi.org/10.1007/s00190-014-0742-8.
- Cataloglu, A., Weimer, L., Eckert, K., et al., 2004. Micro-vibration Verification of GOCE Thermal Hardware. Technical Report 2004–01-2390 SAE International. https://doi.org/10.4271/2004-01-2390.
- Dhadly, M., Emmert, J., Drob, D., et al., 2017. Seasonal dependence of northern high-latitude upper thermospheric winds: a quiet time climatological study based on ground-based and space-based measurements. J. Geophys. Res.: Space Phys. 122 (2), 2619–2644. https://doi.org/10.1002/2016JA023688.
- Dhadly, M.S., Emmert, J.T., Drob, D.P., et al., 2018. Seasonal dependence of geomagnetic active-time northern high-latitude upper thermospheric winds. J. Geophys. Res.: Space Phys. 123 (1), 739–754. https://doi.org/10.1002/2017JA024715.
- Dhadly, M.S., Emmert, J.T., Jones, M., et al., 2020. Oscillations in Neutral Winds Observed by GOCE. Geophys. Res. Lett. 47 (17). https://doi.org/10.1029/2020GL089339.
- Doornbos, E., Bruinsma, S., Koppenwallner, G. et al., 2014. GOCE+ Theme 3: Air density and wind retrieval using GOCE data Final report-updated after CCN 1. Technical Report ESA contract 4000102847/NL/EL European Space Agency.
- Doornbos, E., Den, Van, IJssel, J., Lühr, H., et al., 2010. Neutral density and crosswind determination from arbitrarily oriented multiaxis accelerometers on satellites. J. Spacecr. Rock. 47 (4), 580–589. https://doi.org/10.2514/1.48114.
- Drinkwater, M., Haagmans, R., Muzzi, D. et al., 2007. The goce gravity mission: Esa's first core explorer. In 3rd GOCE User Workshop, 6–8 November 2006, Frascati, Italy ESA SP-627 (pp. 1–7). European Space Agency.
- Drob, D.P., Emmert, J.T., Crowley, G., et al., 2008. An empirical model of the Earth's horizontal wind fields: HWM07. J. Geophys. Res.: Space Phys. 113 (12). https://doi.org/10.1029/2008JA013668.
- Drob, D.P., Emmert, J.T., Meriwether, J.W., et al., 2015. An update to the Horizontal Wind Model (HWM): The quiet time thermosphere. Earth and Space Sci. 2 (7), 301–319. https://doi.org/10.1002/2014EA000089.
- Dumontel, M., 2010. GOCE Stand-alone Aerodynamic Model How-to. Technical Report GOTN AI-0179 ThalesAlenia Space. Issue 1.
- Dutch Space (2005). GOCE Design Definition Document. Technical Report GO-RP-DUS-0002 Dutch Space Leiden, The Netherlands. Issue 4.
- Dutch Space, 2006. GOCE Solar Array: Detailed Thermal Model Analysis. Technical Report GO-RP-DUS-0004 Dutch Space Leiden, The Netherlands. Issue 4.
- Floberghagen, R., Fehringer, M., Lamarre, D., et al., 2011. Mission design, operation and exploitation of the gravity field and steady-state ocean circulation explorer mission. J. Geodesy 85 (11), 749–758. https://doi.org/10.1007/s00190-011-0498-3.
- Fortescue, P., Swinerd, G., Stark, J., 2011) Spacecraft Systems Engineering. (4th ed.). John Wiley & Sons. doi:10.1002/9781119971009.
- Hładczuk, N.A., van den IJssel, J., Kodikara, T., et al., 2024. GRACE-FO radiation pressure modelling for accurate density and crosswind retrieval. Adv. Space Res. 73 (5), 2355–2373. https://doi.org/10.1016/j.asr.2023.12.059.
- van den IJssel, J., Doornbos, E., Iorfida, E., et al., 2020. Thermosphere densities derived from Swarm GPS observations. Adv. Space Res. 65 (7), 1758–1771. https://doi.org/10.1016/j.asr.2020.01.004.
- Kornfeld, R.P., Arnold, B.W., Gross, M.A. et al., 2019. GRACE-FO: The gravity recovery and climate experiment follow-on mission. In J. Spacecr. Rock. (pp. 931–951). AIAA International volume 56. doi:10.2514/1.A34326.
- Li, Z., Ziebart, M., Bhattarai, S., et al., 2018. Fast solar radiation pressure modelling with ray tracing and multiple reflections. Adv. Space Res. 61 (9), 2352–2365. https://doi.org/10.1016/J.ASR.2018.02.019.
- Liu, H., Doornbos, E., Nakashima, J., 2016. Thermospheric wind observed by GOCE: Wind jets and seasonal variations. J. Geophys.

- Res.: Space Phys. 121 (7), 6901–6913. https://doi.org/10.1002/2016JA022938.
- March, G., Doornbos, E.N., Visser, P., 2019a. High-fidelity geometry models for improving the consistency of CHAMP, GRACE, GOCE and Swarm thermospheric density data sets. Adv. Space Res. 63 (1), 213–238. https://doi.org/10.1016/j.asr.2018.07.009.
- March, G., Visser, T., Visser, P., et al., 2019b. CHAMP and GOCE thermospheric wind characterization with improved gas-surface interactions modelling. Adv. Space Res. 64 (6), 1225–1242. https://doi.org/ 10.1016/j.asr.2019.06.023.
- Mishra, R., Militky, J., Venkataraman, M., 2018. Nanoporous materials. In: Nanotechnology in Textiles: Theory and Application. Elsevier, pp. 311–353. https://doi.org/10.1016/B978-0-08-102609-0.00007-9.
- Molina, I., Scherliess, L., 2023. Spatial and temporal correlations of thermospheric zonal winds from GOCE satellite observations. Front. Astron. Space Sci. 10. https://doi.org/10.3389/ fspas.2023.1214591.
- Montenbruck, O., Steigenberger, P., Hugentobler, U., 2015. Enhanced solar radiation pressure modeling for Galileo satellites. J. Geodesy 89 (3), 283–297. https://doi.org/10.1007/s00190-014-0774-0.
- Picone, J.M., Hedin, A.E., Drob, D.P. et al., 2002. NRLMSISE-00 empirical model of the atmosphere: Statistical comparisons and scientific issues. J. Geophys. Res.: Space Phys., 107(A12)(1468). doi:10.1029/2002JA009430.
- Robertson, R.V., Earle, G.D., Bailey, S.M., et al., 2015. Highly Physical Solar Radiation Pressure Modeling During Penumbra Transitions Ph. D. thesis. Virginia Polytechnic Institute and State University Virginia, United States
- Siemes, C., Borries, C., Bruinsma, S., et al., 2023. New thermosphere neutral mass density and crosswind datasets from CHAMP, GRACE, and GRACE-FO. J. Space Weather Space Clim. 13, 16. https://doi. org/10.1051/swsc/2023014.
- Siemes, C., van den IJssel, J., Visser, P., 2024. Uncertainty of thermosphere mass density observations derived from accelerometer and

- GNSS tracking data. Adv. Space Res. https://doi.org/10.1016/j.asr.2024.02.057.
- Silverman, E.M., 1995. Space Environmental Effects on Spacecraft: LEO
   Materials Selection Guide, Part 1. Technical Report NASA CR-4661.
   In: Part 1 TRW Space & Electronics One Space Park, Redondo Beach,
- Valentini, D., Vacance, M., Battaglia, D., et al., 2006. GOCE Instrument Thermal Control. In: Technical Report 2006–01-2044 SAE International. https://doi.org/10.4271/2006-01-2044.
- Vielberg, K., Kusche, J., 2020. Extended forward and inverse modeling of radiation pressure accelerations for LEO satellites. J. Geodesy 94 (4). https://doi.org/10.1007/s00190-020-01368-6.
- Visser, P., van den IJssel, J.A., 2016. Calibration and validation of individual GOCE accelerometers by precise orbit determination. J. Geodesy 90 (1), 1–13. https://doi.org/10.1007/s00190-015-0850-0.
- Visser, T., March, G., Doornbos, E., et al., 2019. Horizontal and vertical thermospheric cross-wind from GOCE linear and angular accelerations. Adv. Space Res. 63 (10), 3139–3153. https://doi.org/10.1016/j.asr.2019.01.030.
- Wang, W., Burns, A.G., Liu, J., 2021. Upper Thermospheric Winds: Forcing, Variability, and Effects. In Space Physics and Aeronomy, Upper Atmosphere Dynamics and Energetics (pp. 41–63). wiley. doi:10.1002/9781119815631.ch3.
- Wang, Y., Li, M., Jiang, K., et al., 2023. Improving Precise Orbit Determination of LEO Satellites Using Enhanced Solar Radiation Pressure Modeling. Space Weather 21 (1). https://doi.org/10.1029/ 2022SW003292.
- Wöske, F., Kato, T., Rievers, B., et al., 2019. GRACE accelerometer calibration by high precision non-gravitational force modeling. Adv. Space Res. 63 (3), 1318–1335. https://doi.org/10.1016/j.asr.2018.10.025.
- Ziebart, M., 2004. Generalized analytical solar radiation pressure modeling algorithm for spacecraft of complex shape. J. Spacecr. Rock. 41 (5), 840–848. https://doi.org/10.2514/1.13097.